

# Scalable hierarchical BayeSN inference: Investigating dependence of SN Ia host galaxy dust properties on stellar mass and redshift

Matthew Grayling<sup>1\*</sup>, Stephen Thorp<sup>2</sup>, Kaisey S. Mandel<sup>1,3</sup>, Suhail Dhawan<sup>1</sup>, Ana Sofia M. Uzsoy<sup>4</sup>, Benjamin M. Boyd<sup>1</sup>, Erin E. Hayes<sup>1</sup> and Sam M. Ward<sup>1</sup>

<sup>1</sup>*Institute of Astronomy and Kavli Institute for Cosmology, Madingley Road, Cambridge CB3 0HA, UK*

<sup>2</sup>*Oskar Klein Centre, Department of Physics, Stockholm University, SE-106 91 Stockholm, Sweden*

<sup>3</sup>*Statistical Laboratory, DPMMS, University of Cambridge, Wilberforce Road, Cambridge, CB3 0WB, UK*

<sup>4</sup>*Center for Astrophysics | Harvard & Smithsonian, Cambridge, MA 02138, USA*

Accepted XXX. Received YYY; in original form ZZZ

## ABSTRACT

We apply the hierarchical probabilistic SED model BayeSN to analyse a sample of 475 SNe Ia ( $0.015 < z < 0.4$ ) from Foundation, DES3YR and PS1MD to investigate the properties of dust in their host galaxies. We jointly infer the dust law  $R_V$  population distributions at the SED level in high- and low-mass galaxies simultaneously with dust-independent, intrinsic differences. We find an intrinsic mass step of  $-0.049 \pm 0.016$  mag, at a significance of  $3.1\sigma$ , when allowing for a constant intrinsic, achromatic magnitude offset. We additionally apply a model allowing for time- and wavelength-dependent intrinsic differences between SNe Ia in different mass bins, finding  $\sim 2\sigma$  differences in magnitude and colour around peak and  $4.5\sigma$  differences at later times. These intrinsic differences are inferred simultaneously with a difference in population mean  $R_V$  of  $\sim 2\sigma$  significance, demonstrating that both intrinsic and extrinsic differences may play a role in causing the host galaxy mass step. We also consider a model which allows the mean of the  $R_V$  distribution to linearly evolve with redshift but find no evidence for any evolution - we infer the gradient of this relation  $\eta_R = -0.38 \pm 0.70$ . In addition, we discuss in brief a new, GPU-accelerated Python implementation of BayeSN suitable for application to large surveys which is publicly available and can be used for future cosmological analyses; this code can be found here: <https://github.com/bayesn/bayesn>.

**Key words:** supernovae: general – surveys

## 1 INTRODUCTION

Type Ia supernovae (SNe Ia) are bright, thermonuclear explosions of carbon-oxygen white dwarfs in a binary system (e.g., see Maguire 2017). They are excellent distance indicators, used for the discovery of the accelerated expansion of the universe (Riess et al. 1998; Perlmutter et al. 1999), and play a central role in precisely constraining the properties of dark energy, e.g. equation of state ( $w$ ), time dependence (Brout et al. 2022; Dark Energy Survey Collaboration et al. 2024). SNe Ia are also crucial for local measurements of the Hubble Constant ( $H_0$ ) via the distance ladder (Riess et al. 2022), which is currently in  $\sim 5\sigma$  tension with the inference from the early universe (Planck Collaboration et al. 2020).

While the current best constraints on  $w$  are dominated by statistical errors (Vincenzi et al. 2024), the advent of upcoming surveys such as the Legacy Survey of Space and Time at Vera Rubin Observatory (LSST; Ivezić et al. 2019) – as well as complementary low-redshifts surveys such as the Young Supernova Experiment (YSE; Jones et al. 2021; Aleo et al. 2023) and Zwicky Transient Facility (ZTF; Bellm et al. 2019a,b) – means systematic uncertainties are becoming increasingly important within supernova cosmology. Improving the constraints on cosmological parameters from SNe Ia hinges on im-

proved physical understanding of the nature of these events. In this paper, we present analysis of a combined sample of 475 SNe Ia using the hierarchical Bayesian SED model BayeSN (Mandel et al. 2022; Thorp et al. 2021), focusing on how their properties vary as a function of both host galaxy stellar mass and redshift. In addition, we present a new GPU-accelerated Python implementation of BayeSN which we make publicly available.

A key open question within the field at present is the nature of the host galaxy ‘mass step’, whereby supernovae in higher mass galaxies are on average brighter than those in lower mass galaxies even after standardisation (Sullivan et al. 2010; Kelly et al. 2010). This effect has been consistently observed in optical samples with a mass step of  $\sim 0.04 - 0.1$  mag (e.g. Kelly et al. 2010; Sullivan et al. 2010; Lampeitl et al. 2010; Gupta et al. 2011; Childress et al. 2013; Betoule et al. 2014; Jones et al. 2018, 2019; Roman et al. 2018; Smith et al. 2020; Kelsey et al. 2021), with the split between high- and low-mass hosts typically placed between  $10^{10} M_\odot$  (e.g. Sullivan et al. 2010) and  $10^{10.8} M_\odot$  (e.g. Kelly et al. 2010). Relations have also been demonstrated between SN luminosity and other environmental properties, including star formation rate (SFR), specific star formation rate (sSFR) and rest-frame colour (e.g. Lampeitl et al. 2010; Sullivan et al. 2010; Briday et al. 2022). Subsequent studies have demonstrated that SN luminosity shows a stronger relation with local properties, derived from the region in which each SN exploded rather than from

\* Contact e-mail: [mg2102@cam.ac.uk](mailto:mg2102@cam.ac.uk)

the whole galaxy (e.g. Rigault et al. 2013, 2015, 2020; Jones et al. 2015; Moreno-Raya et al. 2016a,b; Jones et al. 2018; Kim et al. 2018; Roman et al. 2018; Kim et al. 2019; Rose et al. 2019; Kelsey et al. 2021).

The exact physical cause of the mass step remains open for debate. It could, for example, be a result of intrinsic differences in the SN populations in high- and low-mass galaxies; a number of works have posited that this effect could result from a difference in SN progenitors in different environments (e.g. Sullivan et al. 2010; Childress et al. 2014; Kim et al. 2018; Rigault et al. 2020; Briday et al. 2022). Alternatively, the mass step could arise from extrinsic differences; Brout & Scolnic (2021) proposed that it can be explained entirely by differences in host galaxy dust properties between high- and low-mass SN hosts, requiring no difference in intrinsic SN populations.

Several works have found results consistent with the view that extrinsic effects can explain the mass step. The aforementioned study presented in Brout & Scolnic (2021) finds that a dust parameter  $R_V$  distribution with a mean  $\mu_R$  of  $1.50 \pm 0.25$  for high-mass hosts and  $2.75 \pm 0.35$  for low-mass hosts, along with a wide standard deviation of  $\sigma_R = 1.3 \pm 0.2$ , provides the best match to the SALT2 (Guy et al. 2007) fits of 1445 SNe Ia from the Carnegie Supernova Project I (CSP-I; Contreras et al. 2010; Stritzinger et al. 2011; Krisciunas et al. 2017), the CfA (Hicken et al. 2009, 2012), Foundation (Foley et al. 2018; Jones et al. 2019), the Pan-STARRS-1 Medium Deep Survey (Rest et al. 2014; Scolnic et al. 2018), Supernova Legacy Survey (Astier et al. 2006; Betoule et al. 2014), SDSS-II (Frieman et al. 2008; Sako et al. 2011, 2018) and the Dark Energy Survey (DES; Dark Energy Survey Collaboration et al. 2016; Brout et al. 2019). Popovic et al. (2023) updates the methods of Brout & Scolnic (2021) to perform inference using an MCMC sampler, finding  $\mu_R$  for high- and low-mass hosts of  $2.138 \pm 0.25$  and  $3.026 \pm 0.375$  respectively for the Pantheon+ sample of 1701 SNe Ia (Brout et al. 2022). Wiseman et al. (2023) finds that a model with a galaxy age-varying  $R_V$  and no intrinsic luminosity difference replicates the observed SN population well, although does not rule out that intrinsic differences may play a role in the mass step. Meldorf et al. (2023) analysed the dust laws of 1100 SN host galaxies in DES and found a significant difference in  $R_V$  between high- and low-mass galaxies of  $\sim 0.7$ , albeit this was based on analysis of the attenuation law of the full galaxy rather than focusing on extinction along the line-of-sight to SN positions.

In contrast, a number of other works have instead been consistent with the view that the mass step results at least in part from intrinsic differences. For example, González-Gaitán et al. (2021) finds evidence for a mass step alongside a difference in  $R_V$  values between high- and low-mass galaxies, and posits that this may result from a difference in intrinsic colour. In a separate analysis of attenuation laws of SN host galaxies in DES, Duarte et al. (2023) found that host galaxy dust differences cannot fully explain the mass step. Jones et al. (2023) presented a version of the SALT3 model (Kenworthy et al. 2021) which split the training set as a function of host galaxy stellar mass, finding evidence for differences in spectroscopic and photometric properties of SNe Ia between each bin, although in the latter case the model could not discern intrinsic differences from those caused by dust. Recent analysis of the DES-SN 5YR sample of SNe Ia from DES (Dark Energy Survey Collaboration et al. 2024) found inconsistencies between parameters inferred from simulations based on a dust-only mass step and those inferred from real data, suggesting that dust alone cannot explain the mass step (Vincenzi et al. 2024).

Additionally, if the mass step were solely a result of host galaxy dust, one would expect that no mass step would be observed in near-infrared (NIR) wavelengths where dust – particularly the value of  $R_V$

– has little effect. Despite this, several works have found evidence for a mass step in NIR wavelengths. Ponder et al. (2021) analysed 143 SNe Ia in  $H$ -band and found a significant step of  $0.13 \pm 0.04$  at a mass of  $10^{10.43} M_\odot$ ; omitting notable outliers, the most significant step is  $0.08 \pm 0.04$  at  $10^{10.65} M_\odot$ . Uddin et al. (2020) analysed a sample of 113 SNe Ia from CSP-I, fitting them using the MAX\_MODEL method within SNOOPY (Burns et al. 2011) across  $uBgVriYJH$  bands. Based on a split at the median stellar mass of the sample,  $10^{10.65} M_\odot$ , they find an  $H$ -band step of  $0.093 \pm 0.043$  mag and a  $J$ -band step of  $0.090 \pm 0.043$  mag – overall, they find NIR steps of comparable significance to the optical steps and that the relation between step size and wavelength was inconsistent with a dust-driven step. Jones et al. (2022) analysed a sample of 79 SNe, including 42 low redshift SNe ( $z < 0.1$ ) from CSP-I and 37 higher redshift ( $0.2 < z < 0.7$ ) SNe with rest-frame NIR, and found a mass step from NIR light curves of  $0.072 \pm 0.041$  mag at mass of  $10^{10.44} M_\odot$ .

However, it should be noted that other NIR analyses have not found evidence for a mass step. Johansson et al. (2021) analysed a sample of  $\sim 240$  SNe Ia using the COLOUR\_MODEL method within SNOOPY, assuming a fixed host galaxy  $R_V = 2.0$ . This study finds NIR mass steps in  $J$  and  $H$ -bands of  $0.021 \pm 0.033$  mag and  $-0.020 \pm 0.036$  respectively, both consistent with zero, although not inconsistent with the steps found in Uddin et al. (2020) considering the uncertainties. They also find the mass step to be consistent with zero across optical and NIR bands when allowing  $R_V$  to be a free parameter for each SN.

Most recently, Uddin et al. (2023) analysed a sample of 325 SNe from CSP-I and CSP-II (Phillips et al. 2019), including the sample of 113 SNe analysed in Uddin et al. (2020). Using a more recent version of the MAX\_MODEL method within SNOOPY, they find no significant mass step in any optical or NIR band, with the possible exception of  $u$ -band which shows a step of  $-0.151 \pm 0.069$  mag. They also demonstrate that their inferred correlations between host mass and luminosity do not vary with wavelength. Both of these findings are consistent whether using only the CSP-I sample from Uddin et al. (2020) or the combined CSP-I and CSP-II sample. Additionally, Karchev et al. (2023a) applied Bayesian model comparison using simulation-based inference (SBI) and found results disfavouring both intrinsic and extrinsic differences.

The debate between a mass step driven by extrinsic effects and intrinsic variation in the SN population closely relates to a general challenge in SNe Ia – disentangling the intrinsic distribution from the effects of host galaxy dust extinction. It is challenging, for example, to tell apart an intrinsically red SN from an intrinsically typical SN which happened to explode in a dusty environment. SALT (Guy et al. 2007; Kenworthy et al. 2021) is the most widely used model for SN Ia analyses, however a key limitation is that it compresses all colour information into a single  $c$  parameter, which roughly corresponds to peak  $B - V$  apparent colour. As demonstrated in Mandel et al. (2017), with this approach care must be taken to avoid confounding intrinsic variation with dust. While some SALT-based analyses do break down the  $c$  parameter into separate intrinsic and dust components (e.g. Mandel et al. 2017; Brout & Scolnic 2021; Popovic et al. 2023), SALT is trained with a single colour law describing the effect that the apparent colour parameter  $c$  has on the underlying SN SED, meaning that it cannot accommodate the possibility of different dust laws when fitting observed light curves.

Unlike SALT, SNOOPY does include an explicit treatment of dust extinction. However, in addition to host galaxy dust it is also important to incorporate the intrinsic colour distribution of SNe, including variations beyond those correlated with light curve shape. Excluding this effect can bias estimates of  $R_V$  (Mandel et al. 2017) and lead to

overestimates of the colour variation caused by an  $R_V$  distribution (Thorp & Mandel 2022).

The challenge of disentangling dust from intrinsic SN variation has led to the development of hierarchical Bayesian models for analysing samples of SNe Ia. Hierarchical modelling was first applied to this end in Mandel et al. (2009, 2011) and again in Burns et al. (2014); the former method has since been developed further into the hierarchical SED model BayeSN (Thorp et al. 2021; Mandel et al. 2022). The advantage of a hierarchical approach is that it allows for joint inference of population level and individual SN parameters. Specific to this problem, it allows for explicit, separate treatments of the intrinsic and host galaxy dust distributions of SNe Ia, with the population-level parameters inferred while marginalising over all individual SN (latent) parameters. Hierarchical modelling also provides more precise inference of the width of a population, when compared with simply taking the standard deviation of a number of individual estimates; the latter approach will lead to overestimates as it fails to take into account errors on the individual estimates (see discussion in Section 5 of Thorp & Mandel 2022). Wojtak et al. (2023) presents a recent analysis of SNe Ia using hierarchical Bayesian modelling, finding evidence for two separate populations although not splitting the population directly based on host galaxy stellar mass.

Both Thorp et al. (2021) and Thorp & Mandel (2022) apply BayeSN to study the dust distributions of SNe in high- and low-mass hosts and find no evidence for a difference in  $R_V$  distributions between different environments. Notably, Thorp & Mandel (2022) finds evidence for a NIR mass step even when allowing for different dust distributions between high- and low-mass hosts.

In this work, we use a new GPU-accelerated implementation of BayeSN which has increased performance by factors of  $\sim 50$ -100, making large-scale hierarchical analyses of SNe Ia more than feasible; we make this code publicly available. We build on previous analysis in Thorp et al. (2021) in applying BayeSN to optical data to study the host galaxy dust properties of SNe Ia. We apply the model trained in Thorp et al. (2021) to higher redshift SNe from the Dark Energy Survey three-year sample (DES3YR) and the Pan-STARRS Medium Deep survey (PS1MD), increasing both the sample size and redshift range covered. We investigate the host galaxy dust distributions in both high- and low-mass hosts in tandem with dust-independent intrinsic differences, allowing us to comment on the debate between intrinsic and extrinsic causes. We also perform the first hierarchical Bayesian analysis with a redshift-dependent  $R_V$  distribution to test whether there is any evidence that SN host galaxy dust properties evolve with redshift.

In Section 2, we detail the SN samples used in this work and describe redshift cuts applied to mitigate for selection effects. In Section 3, we summarise the BayeSN model and our new GPU-accelerated implementation, as well as detailing the specific models and analysis variants used within this work. We then describe our results, looking separately at a single dust population (Section 4.1), multiple dust populations split by host galaxy stellar mass (Section 4.2) and a redshift-dependent dust distribution (Section 4.3), before concluding in Section 5.

## 2 DATA

For this work we analyse three separate spectroscopically-confirmed optical samples of SNe Ia observed in *griz* bands: the Foundation DR1 sample (Foley et al. 2018), the Dark Energy Survey (DES; Dark Energy Survey Collaboration et al. 2016) 3-year sample (DES3YR; Brout et al. 2019; Smith et al. 2020) and the sample from the Pan-

STARRS Medium Deep survey (PS1MD; Kaiser et al. 2010) as compiled in the Pantheon sample (Scolnic et al. 2018). For all three samples, we use photometric data taken from the Pantheon+ compilation (Scolnic et al. 2022), which corrects for cross-calibration systematics between surveys. We include SNe from PS1MD present in the Pantheon compilation, rather than the Pantheon+ compilation, to increase our sample size as there were a few objects which were removed in the latter compilation that are suitable for our analysis.

All of the SNe in this analysis pass standard cosmology cuts (e.g. Scolnic et al. 2018, 2022) and have global host galaxy masses measured from SED fits to *ugrizy* and *ugriz* photometry for Foundation (Jones et al. 2019) and PS1MD (Scolnic et al. 2018), and from DES *griz* photometry for DES3YR (Brout et al. 2019; Smith et al. 2020; Wiseman et al. 2020).

Foundation DR1 is a local sample; we apply the same selection cuts as used in Thorp et al. (2021) for a total of 157 SNe Ia which span a redshift range of  $0.015 < z < 0.08$ . In contrast, DES3YR and PS1MD are higher redshift meaning that they will be strongly influenced by selection effects such as Malmquist bias (Malmquist 1922). DES3YR comprises 207 SNe Ia over a redshift range of  $0.077 < z < 0.85$ , while PS1MD comprises 279 SNe Ia over a range of  $0.026 < z < 0.63$ . To mitigate for this, in this work we take volume limited subsets of the full samples - we apply a cut at the point where the redshift distribution begins to decrease, indicating that a large number of SNe have been missed due to selection effects. For DES3YR, we apply a redshift cut at 0.4 to give a sample of 119 SNe Ia, while for PS1MD we apply a cut at 0.35 for a final sample of 199 SNe Ia. When combined, these samples include a total of 475 SNe Ia. Figure 1 shows the redshift distributions of the three samples used in this work, with dashed lines indicating the upper redshift cuts applied to DES3YR and PS1MD. For discussion of these redshift cuts, please see Appendix B. In brief, we investigate how the total *V*-band extinction varies with redshift and find no evidence that these volume limited sub-samples are significantly impacted by selection effects, although cannot rule out that some small effects may remain.

It should be noted that in this work we utilise the version of the BayeSN model presented in Thorp et al. (2021), which is defined down to a rest-frame wavelength of 3500 Å, while the redshift range spanned by DES3YR and PS1MD means that rest-frame *g*-band often covers wavelengths below this lower limit. As such, for the majority of SNe in these two samples we disregard *g*-band data.

## 3 METHOD

For this work, we utilise the hierarchical Bayesian SN Ia SED model BayeSN (Thorp et al. 2021; Mandel et al. 2022). Hierarchical Bayes provides an ideal framework for joint inference of populations and the individual objects which comprise them, for example looking in tandem at individual SN host galaxies and the overall population. In this section we detail the model used for our analysis and discuss the different variants used.

### 3.1 Numpyro Implementation of BayeSN

Compared with previous BayeSN analyses (e.g. Mandel et al. 2022; Thorp et al. 2021; Thorp & Mandel 2022; Ward et al. 2023b; Dhawan et al. 2023) which implemented the model in STAN (Carpenter et al. 2017; Stan Development Team 2023), we use a version implemented using the probabilistic programming Python library NUMPYRO (Phan et al. 2019; Bingham et al. 2019). All computations in NUMPYRO are carried out using JAX (Bradbury et al. 2018), meaning that this

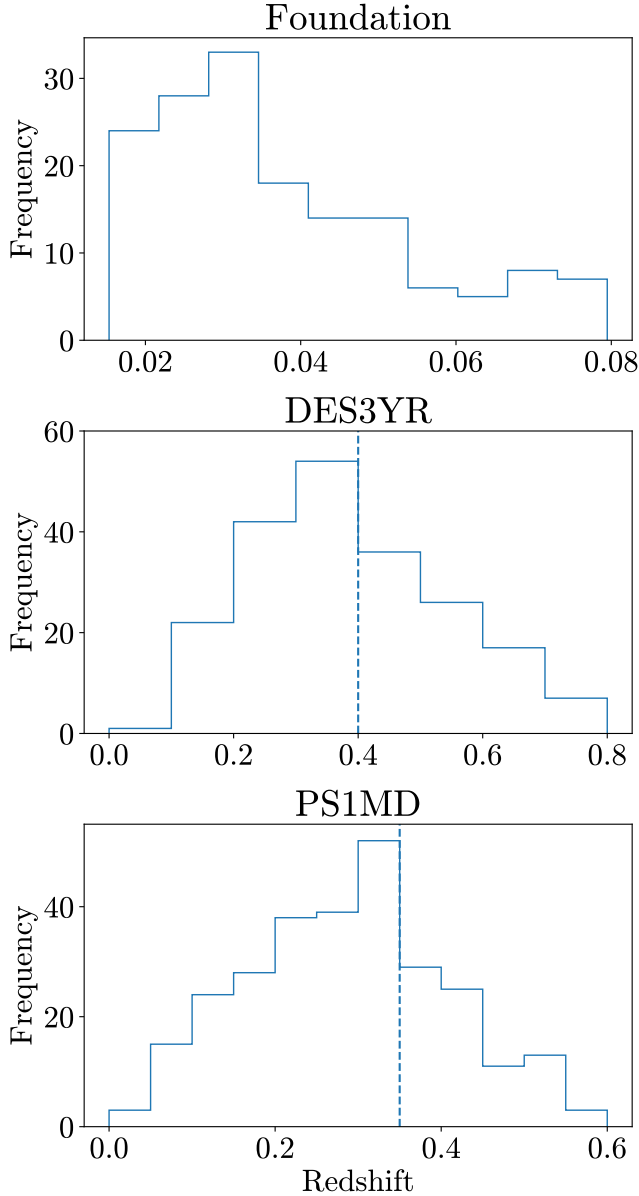


**Figure 1.** Redshift distributions for the 3 samples used in this work; Foundation, DES3YR and PS1MD. Dashed lines for DES3YR and PS1MD indicate the upper redshift limit of the volume limited sub-samples included in our analysis.

implementation of BayeSN supports just-in-time (JIT) compilation and GPUs, and similarly to the STAN version is fully differentiable with autodiff. By combining vectorised likelihood evaluation across the SN population with the use of GPU acceleration, the speed of the inference has increased by factors of  $\sim 50$ -100, enabling hierarchical analyses of much larger SN samples. The NUMPYRO implementation of the BayeSN model can be found here: <https://github.com/bayesn/bayesn>.

BayeSN uses the NUMPYRO implementation of the No U-Turn Sampler (NUTS; Hoffman & Gelman 2014), an adaptive variant of Hamiltonian Monte Carlo (HMC; Neal 2011; Betancourt 2017), to sample from target posterior distributions. To give an example of typical performance, for the hierarchical SED- and population-

level dust models presented in this work HMC typically converges and generates sufficient effective sample sizes in  $\sim 15$ -30 minutes; these values are quoted for 4 chains run in parallel across 4 NVIDIA A100 GPUs, using resources from the Cambridge Service for Data Driven Discovery (CSD3). This runtime allows for quick exploration of different model variants.

While this work focuses on the physical properties of the SN Ia population and does not touch on cosmological analysis (as discussed in Section 3.2.2 our results are conditioned on a fixed cosmology), the BayeSN code we make available can also be used to infer distance. A model is first ‘trained’ by inferring the population-level parameters of the model (as in Mandel et al. 2022; Thorp et al. 2021; Ward et al. 2023b). These population-level parameters are then fixed and the model can be applied to infer a cosmology-independent distance modulus  $\mu^s$  simultaneously with all the other latent SN parameters, conditioned on those fixed population parameters. Using this approach, distance is jointly inferred with SN latent parameters rather than being estimated via the Tripp formula (Tripp 1998) – a post-hoc linear relation with those SN parameters – as in SALT-based analyses. The advantage of this method is that it allows the full SN light curve to be used when estimating distance rather than compressing it to a single colour at peak, and also provides a distance estimate separately marginalised over the intrinsic and extrinsic variation observed in the population. Work is underway to integrate our code within the SN analysis framework SNANA (Kessler et al. 2009), and future cosmological analyses will be able to use BayeSN-derived distances.

### 3.2 The BayeSN Model

BayeSN is an SED model for SNe Ia, with the full time- and wavelength-varying SED given by,

$$-2.5 \log_{10}[S_s(t, \lambda_r)/S_0(t, \lambda_r)] = M_0 + W_0(t, \lambda_r) + \delta M^s + \theta_1^s W_1(t, \lambda_r) + \epsilon^s(t, \lambda_r) + A_V^s \xi(\lambda_r; R_V^{(s)}) \quad (1)$$

where  $t$  is the rest-frame phase relative to B-band maximum and  $\lambda_r$  is rest-frame wavelength.  $S_0(t, \lambda_r)$  is the optical-NIR SN Ia SED template of Hsiao et al. (2007) and is fixed a priori as a zeroth-order template, along with the normalisation constant  $M_0$  which is set to  $-19.5$ . All parameters denoted with  $s$  are latent SN parameters, with unique values for each SN  $s$ , while all other parameters are global hyperparameters shared across the population. The different components which make up the model are described as follows:

- $W_0(t, \lambda_r)$  is a function that warps and normalises the zeroth-order SED template to create a mean intrinsic SED for the population, while  $W_1(t, \lambda_r)$  is a functional principal component (FPC) that describes the first mode of intrinsic SED variation for SNe Ia. Both of these are implemented as cubic spline surfaces.

- $\theta_1^s$  is a coefficient quantifying the effect of the  $W_1$  FPC for each SN. This is modelled as a normal distribution, with  $\theta_1^s \sim N(0, 1)$ . Combined,  $W_1(t, \lambda_r)$  and  $\theta_1^s$  capture the ‘broader-brighter’ relation observed in SNe Ia where intrinsically brighter light curves evolve over longer timescales around peak (Phillips 1993).

- $\delta M^s$  is an achromatic, time-independent magnitude offset for each SN, drawn from a normal distribution with  $\delta M^s \sim N(0, \sigma_0^2)$ .  $\sigma_0$  is a hyperparameter describing the width of this distribution and is inferred when the model is trained.

- $\epsilon^s(t, \lambda_r)$  is a time- and wavelength-dependent function that describes the time-varying residual intrinsic colour variations in the SED not captured by  $\theta_1^s W_1(t, \lambda_r)$ . This parameter is represented by a cubic spline function over time and wavelength defined by a

matrix of knots  $\mathbf{E}^s$ . These are drawn from a multivariate Gaussian  $\mathbf{e}^s \sim N(0, \Sigma_\epsilon)$ , where  $\mathbf{e}^s$  is the vectorisation of the  $\mathbf{E}^s$  matrix. The covariance matrix  $\Sigma_\epsilon$  is a hyperparameter of the model which describes the distribution of residual scatter across the population of SNe Ia and is inferred during training.

•  $A_V^s$  and  $R_V^{(s)}$  describe the host galaxy extinction law for each SN;  $A_V^s$  is the total amount of V-band extinction, while  $R_V^{(s)}$  parameterises the Fitzpatrick (1999) dust extinction law assumed by the model.  $R_V^{(s)}$  can be treated as either a shared parameter across the population or a unique value for each SN (see Section 3.2.3 for discussion of different assumed  $R_V^s$  distributions). For  $A_V^s$ , we assume an exponential prior described by a scale parameter  $\tau_A$ , such that  $A_V^s \sim \text{Exp}(\tau_A)$ .

The rest-frame, host galaxy dust-extinguished SED model  $S_s(t, \lambda_r)$  is then scaled based on distance modulus  $\mu^s$ , redshifted and corrected for Milky Way dust extinction using a Fitzpatrick (1999) dust law with  $R_V = 3.1$  and dust maps from Schlafly & Finkbeiner (2011). This produces an observer-frame SED, which can be integrated through photometric filters to produce model photometry that can in turn be compared with observed photometry to compute a likelihood. This hierarchical model is trained by inferring all global parameters and latent parameters for a population of SNe Ia (see Mandel et al. (2022) and Thorp et al. (2021) for full discussion of model training). The latent parameters are marginalised over and posterior estimates are obtained for the global parameters.

### 3.2.1 Hierarchical Dust Model

The focus of this analysis is to study the host galaxy dust distributions of the sample. In this work, we modify the BayeSN model discussed previously by fixing all global parameters not related to host galaxy dust extinction ( $W_0, W_1, \Sigma_\epsilon$ ). These parameters are fixed to the values for the T21 model presented in Thorp et al. (2021), which was trained on the sample of 157 SNe from Foundation DR1 also included in this work.

The hyperparameters inferred in our hierarchical model are the mean and standard deviation of the host galaxy  $R_V$  population distribution ( $\mu_R$  and  $\sigma_R$ ) as well as the population mean extinction value ( $\tau_A$ ) and the intrinsic achromatic SN scatter ( $\sigma_0$ ). We place a uniform hyperprior on  $\mu_R$  of  $\mu_R \sim U(1.2, 6)$ . For  $\sigma_R$  we use a half-normal hyperprior with a scale factor of 2 [ $\sigma_R \sim \text{Half-N}(0, 2^2)$ ], following Thorp et al. (2021)<sup>1</sup>. For  $\tau_A$  and  $\sigma_0$ , we adopt half-Cauchy priors with scale parameters of 1.0 mag and 0.1 mag respectively to reflect the expected scales of these parameters, as in Mandel et al. (2022).

### 3.2.2 Conditioning on Distance

There are two approaches that can be taken with regard to distance in this type of hierarchical model, as discussed in Thorp & Mandel (2022). The first is to condition on distance based on redshifts and an assumed cosmology, while the second is to keep photometric distance as a free parameter and marginalise over the distance to each SN  $\mu^s$  when inferring dust hyperparameters. The latter can be advantageous as it provides a cosmology-independent dust estimate,

but effectively means that dust properties are inferred using colour information alone rather than colour and magnitude information. For an optical plus NIR analysis such as Thorp & Mandel (2022), this is sufficient as optical-NIR colours provide additional constraints on the dust law. However, for an optical-only analysis it is necessary to condition on redshift-based distances to obtain reasonable dust constraints.

In this work, we condition on the redshift-distance relation such that the external constraint on  $\mu^s$  is<sup>2</sup>,

$$\mu^s | z^s \sim N(\mu_{\Lambda\text{CDM}}(z^s), \sigma_{\text{ext}}^2) \quad (2)$$

where  $z^s$  is the redshift of each SN,  $\mu_{\Lambda\text{CDM}}(z)$  is the distance modulus of redshift  $z$  assuming a flat  $\Lambda\text{CDM}$  cosmology with  $\Omega_m = 0.28$  and  $H_0 = 73.24 \text{ km s}^{-1} \text{ Mpc}^{-1}$  and  $\sigma_{\text{ext},s}$  is the uncertainty in  $\mu_{\Lambda\text{CDM}}(z^s)$ . This is based on propagating the uncertainty in the spectroscopic redshift  $z^s$  through to an uncertainty in  $\mu$ . The redshift uncertainty is given by the individual uncertainty  $\sigma_z^s$  added in quadrature with a peculiar velocity dispersion  $\sigma_{\text{pec}}$ . In this work, we assume  $\sigma_{\text{pec}} = 150 \text{ km s}^{-1}$  (Carrick et al. 2015)<sup>3</sup>. All posteriors presented in this work are conditioned on this fixed cosmology.

### 3.2.3 Impact of Truncated Dust $R_V$ Population Distribution

As discussed in Section 1, a number of previous studies have applied a population distribution to model host galaxy  $R_V$  for supernovae. One approach would be to model the population as a normal distribution,

$$R_V^s \sim N(\mu_R, \sigma_R^2). \quad (3)$$

However, previous works have typically used a truncated normal distribution to ensure that  $R_V$  cannot go to unphysically low values. For example, Brout & Scolnic (2021) used a distribution truncated at 0.5 at the lower end. A more physically-motivated lower bound on the value of  $R_V$  is 1.2, based on the Rayleigh scattering limit (Draine 2003). We adopt this value for this analysis, modelling the host galaxy  $R_V$  distribution as

$$R_V^s \sim TN(\mu_R, \sigma_R^2, 1.2, \infty), \quad (4)$$

where  $TN(\mu, \sigma^2, a, b)$  denotes a truncated normal distribution with  $\mu$  and  $\sigma^2$  representing the mean and variance of a normal distribution, and  $a$  and  $b$  representing the upper and lower bounds of truncation applied to that normal distribution. This is the  $R_V$  distribution we use throughout our analysis.

However, it is important to note that using a truncated distribution will impact inference in two ways:

(i) Depending on the values of  $\mu_R$  and  $\sigma_R$ , it is important to consider them as fitting parameters rather than directly as the population mean and standard deviation, which we will refer to hereafter as  $\mathbb{E}[R_V]$  and  $\sqrt{\text{Var}[R_V]}$ . Using Eq. 4 with  $\mu_R = 1.2$  will give a half-normal distribution;  $\mathbb{E}[R_V]$  will be significantly different from  $\mu_R$ . Considering a different case, for example where  $\mu_R = 3.0$  and  $\sigma_R = 0.2$ , the truncation can also have minimal effect –  $\mu_R$  and  $\sigma_R$  will be practically identical to  $\mathbb{E}[R_V]$  and  $\sqrt{\text{Var}[R_V]}$ . The relation between  $\mu_R, \sigma_R, \mathbb{E}[R_V]$  and  $\sqrt{\text{Var}[R_V]}$  is detailed in Appendix C.

<sup>1</sup> In our analysis, we find that in some cases the data does not provide strong constraint on the value of  $\sigma_R$ . We do consider the use of different of narrower hyperpriors on  $\sigma_R$  to examine the prior dependence on our posteriors, but find that this has minimal impact on our analysis so opt to focus solely on a scale factor of 2 within this work.

<sup>2</sup> Throughout this paper, we use the notation  $x \sim N(\mu, \sigma^2)$  where  $\mu$  is the mean and  $\sigma^2$  is the variance.

<sup>3</sup> We use this value for consistency with previous BayeSN analyses although note that the use of a higher value e.g.  $300 \text{ km s}^{-1}$  does not impact our conclusions regarding dust. A higher peculiar velocity dispersion trades off slightly against the inferred value of  $\sigma_0$ .

(ii) A truncated  $R_V$  distribution will impact inference of  $\sigma_R$ . In general, unphysically low values of  $R_V$  will lead to poor quality light curve fits since they do not represent realistic extinction laws. Using a normal distribution without truncation rules out larger values of  $\sigma_R$  to ensure that these low  $R_V$  values are not included in the distribution. With a truncated  $R_V$  distribution, these larger  $\sigma_R$  values are not ruled out since low  $R_V$  values are already excluded - a large  $\sigma_R$  will only impact the upper end of the distribution. Overall, the use of a truncated distribution can lead to higher inferred values of  $\sigma_R$ , compared with an untruncated distribution.

The extent to which both of these effects will impact the analysis depends on the values of  $\mu_R$  and  $\sigma_R$ . If the true  $R_V$  distribution is far above the lower limit, the impact will be negligible. If the true distribution overlaps significantly with this lower bound, the truncation will have a significant impact.

### 3.2.4 Assessing Quality of MCMC Chains

We use a number of standard diagnostics to assess the quality of our MCMC chains. We initialise 4 independent chains at different points of parameter space and run them independently, and verify that the chains have mixed and converged using the  $\hat{R}$  (Gelman–Rubin) statistic as well as assessing the effective sample size (Gelman & Rubin 1992; Vehtari et al. 2021). In addition, we check that our chains do not contain any divergent transitions (e.g. Betancourt et al. 2014; Betancourt 2017).

## 3.3 Analysis Variations

Throughout this analysis, we perform a number of variations of our dust inference model, which are detailed as follows.

### 3.3.1 Single Dust Population

We first consider that all SNe are drawn from the same host galaxy dust distribution, with the same priors on  $R_V^s$  and  $A_V^s$  used across all SNe. For this approach, we consider each of the Foundation, DES3YR and PS1MD subsamples separately as well as considering one combined sample including all SNe.

### 3.3.2 Binned Populations

Motivated by ongoing debate regarding the cause of the mass step, we also consider a variation of the model where the dust population hyperparameters are binned based on global host galaxy mass. For example, using this binned approach and assuming a truncated normal distribution, the host galaxy  $R_V$  distributions become

$$R_V^s \sim \begin{cases} TN(\mu_{R,\text{HM}}, \sigma_{R,\text{HM}}^2, 1.2, \infty), & \text{if } M_*^s > M_{\text{split}} \\ TN(\mu_{R,\text{LM}}, \sigma_{R,\text{LM}}^2, 1.2, \infty), & \text{if } M_*^s < M_{\text{split}} \end{cases} \quad (5)$$

where  $M_*^s$  is the host stellar mass of each SN  $s$  and  $M_{\text{split}}$  is some reference stellar mass at which the split point is located. Such a split is also applied to give separate  $A_V$  distributions for high- and low-mass galaxies described by different  $\tau_A$  parameters. In this work, we set  $M_{\text{split}}$  at  $10^{10} M_\odot$ .

In addition, we include parameters which represent a possible intrinsic difference between the populations of SNe Ia in each mass bin. This is done so that the model is flexible enough to allow either a mass step driven by differences in dust properties, some other intrinsic effect, or some combination thereof. We consider three separate forms for this intrinsic mass step, described as follows:

(i) A model including mass step parameters  $\Delta M_{0,\text{HM}}$  and  $\Delta M_{0,\text{LM}}$  which act as a constant achromatic shift in magnitude for each bin applied to the mean of the  $\delta M^s$  distributions, such that

$$\delta M^s \sim \begin{cases} N(\Delta M_{0,\text{HM}}, \sigma_{0,\text{HM}}^2), & \text{if } M_*^s > M_{\text{split}} \\ N(\Delta M_{0,\text{LM}}, \sigma_{0,\text{LM}}^2), & \text{if } M_*^s < M_{\text{split}}. \end{cases} \quad (6)$$

(ii) A model including mass step parameters  $\Delta W_{0,\text{HM}}$  and  $\Delta W_{0,\text{LM}}$ , which allow for a time- and wavelength-dependent difference in the baseline intrinsic ( $\theta_1 = 0$ ) SED, independent of stretch, between SNe in different environments. Throughout our analysis, we use the term baseline to refer to the intrinsic SED with  $\theta_1 = 0$ , since for a population which has a non-zero mean value of  $\theta$  this does not necessarily correspond to the population mean. In this model,

$$W_0 = \begin{cases} W_0^{\text{T21}} + \Delta W_{0,\text{HM}} & \text{if } M_*^s > M_{\text{split}} \\ W_0^{\text{T21}} + \Delta W_{0,\text{LM}} & \text{if } M_*^s < M_{\text{split}} \end{cases} \quad (7)$$

where  $W_0$  describes the baseline intrinsic SED as in Equation 1,  $W_0^{\text{T21}}$  represents the  $W_0$  matrix inferred in Thorp et al. (2021) across SNe Ia in both high- and low-mass galaxies and  $\Delta W_{0,\text{HM}}$  and  $\Delta W_{0,\text{LM}}$  encode a shift in the baseline intrinsic SED in each environment. This more general model in principle also allows for the previous case of a constant, achromatic magnitude shift if that is what the data supports.

(iii) A model which does not include any parameters representing an intrinsic mass step and includes splits only on dust parameters.

The first case allows for the possibility of an intrinsic, achromatic mass step between SNe in high- and low-mass galaxies, as explored in Thorp et al. (2021); Thorp & Mandel (2022). However, this form carries with it the assumption that the baseline intrinsic colour of SNe Ia is the same between high- and low-mass environments. While this is a possibility, the most general and flexible model we explore is one that allows for the baseline intrinsic SED of SNe Ia to vary between high- and low-mass galaxies, which is the second case we explore. It is important to jointly consider intrinsic colour along with the dust distribution since dust extinction is inferred with respect to intrinsic properties.

In the first case, for  $\Delta M_{0,\text{HM}}$  and  $\Delta M_{0,\text{LM}}$  we assume a uniform hyperprior in the range  $[-0.2, 0.2]$  as in Thorp et al. (2021) to safely capture the full range of mass steps observed in previous studies. The total achromatic mass step  $\Delta M_0$  is then given by  $\Delta M_{0,\text{HM}} - \Delta M_{0,\text{LM}}$ . This must be parameterised as a separate parameter for each mass bin to avoid arbitrarily setting one bin to the mean absolute magnitude of the T21 BayeSN model.

In the second case, we assume that the shift in  $W_0$  is a small variation around the overall population baseline intrinsic SED; for all of the elements that compose the  $\Delta W_{0,\text{HM/LM}}$  matrix, we use the hyperprior

$$\Delta W_{0,\text{HM/LM}} \sim N(\mathbf{0}, 0.1 \times \mathbf{I}), \quad (8)$$

where  $\mathbf{I}$  is the identity matrix. The factor of 0.1 represents our expectation that this effect is small<sup>4</sup>.

In the third case, we only include splits on dust parameters between different environments with no parameters representing an intrinsic mass step, effectively enforcing a mass step which is explained by dust properties. This is the approach used by Brout & Scolnic (2021); Popovic et al. (2021) and we include this case for comparison with these works and to examine the effect omitting these parameters has on dust inference.

<sup>4</sup> Relaxing this expectation and allowing a wider prior does not impact our conclusions.

### 3.3.3 Redshift Evolution

The samples we consider in this analysis range in redshift from 0.015 up to 0.4, factoring in the redshift cuts applied to mitigate for selection effects. The range spanned means that these SNe provide an opportunity to test whether there is any evidence that the SN Ia host galaxy dust distribution varies with redshift. To this end we apply a simple linear model for  $\mu_R$ . We adapt Eq. 4, setting

$$\mu_R = \mu_R(z) = \eta_R \times z + \mu_{R,z0} \quad (9)$$

where  $z$  is redshift,  $\eta_R$  is the gradient of the relation between redshift and  $\mu_R$ , and  $\mu_{R,z0}$  is the value of  $\mu_R$  at  $z = 0$ . Within the inference, the prior on a SN at redshift  $z^s$  is then  $R_V^s \sim TN(\mu_R(z^s), \sigma_R^2, 1.2, \infty)$ . We choose a linear model for this relation as the gradient parameter  $\eta_R$  provides a simple way to assess whether the data provides evidence for evolution with redshift i.e. that  $\eta_R$  is non-zero. We also apply a similar linear relation with redshift to  $\tau_A$ , with the value of  $\tau_A$  at  $z = 0$  denoted by  $\tau_{A,z0}$  and the gradient of the relation given by  $\eta_\tau$ . For  $\sigma_R$ , we are often only able to obtain upper limits and judge that we would not be able to constrain a  $\sigma_R$  redshift relation. We elect to keep  $\sigma_R$  as a fixed population parameter and only allow  $\mu_R$  and  $\tau_A$  to vary with redshift.

We use a joint prior on  $\mu_{R,z0}$  and  $\eta_R$ . For  $\mu_{R,z0}$  we use the same prior as applied for  $\mu_R$  previously. For  $\eta_R$ , we apply a uniform prior,

$$\eta_R | \mu_{R,z0} \sim U(1.2 - \mu_{R,z0}, 6 - \mu_{R,z0}). \quad (10)$$

This enforces the condition that  $\mu_R$  is restricted to the range [1.2, 6] below  $z = 1$ , regardless of  $\mu_{R,z0}$ , to rule out unphysical redshift evolution in the  $R_V$  distribution. For  $\tau_{A,z0}$ , we use the same hyperprior as for  $\tau_A$  in Section 3.2.1. For  $\eta_\tau$ , we place a wide uninformative hyperprior such that  $\eta_\tau \sim U(-0.5, 0.5)$  mag, chosen to prevent the posterior distribution from approaching the prior bounds.

## 4 RESULTS AND DISCUSSION

In this section we present and discuss our results for each of our model variations. To demonstrate typical light curve fits obtained using BayeSN, Figure 2 shows examples of a fit to a SN from each of the three surveys which make up our combined sample.

### 4.1 Population Sub-sample Dust Properties

We begin by considering each of the DES, Foundation and PS1MD samples separately, as well as a combined sample containing all SNe across the three samples. The full results are shown in Table 1.

Individually, we obtain  $\mu_R$  values of  $2.66 \pm 0.13$ ,  $3.14 \pm 0.59$  and  $1.69 \pm 0.33$  for Foundation, DES3YR and PS1MD respectively. The differences seen here perfectly highlight the importance of considering the population mean  $\mathbb{E}[R_V]$  as well as just  $\mu_R$  when using a truncated distribution. The inferred value of  $\mu_R = 1.69 \pm 0.33$  for PS1MD is close to the lower truncation bound of 1.2, and therefore a difference between  $\mathbb{E}[R_V]$  and  $\mu_R$  is expected. When we calculate  $\mathbb{E}[R_V]$  for these samples, we instead infer  $2.66 \pm 0.13$ ,  $3.41 \pm 0.57$  and  $2.44 \pm 0.29$  respectively for Foundation, DES3YR and PS1MD, showing PS1MD to be much more consistent with the others. While there is a numerical difference between DES3YR and PS1MD close to 1, considering the uncertainties all three of these samples are statistically consistent with each other and also with the inferred  $\mathbb{E}[R_V]$  value of the combined population,  $2.58 \pm 0.14$ .

The effect of the truncated distribution is also demonstrated in

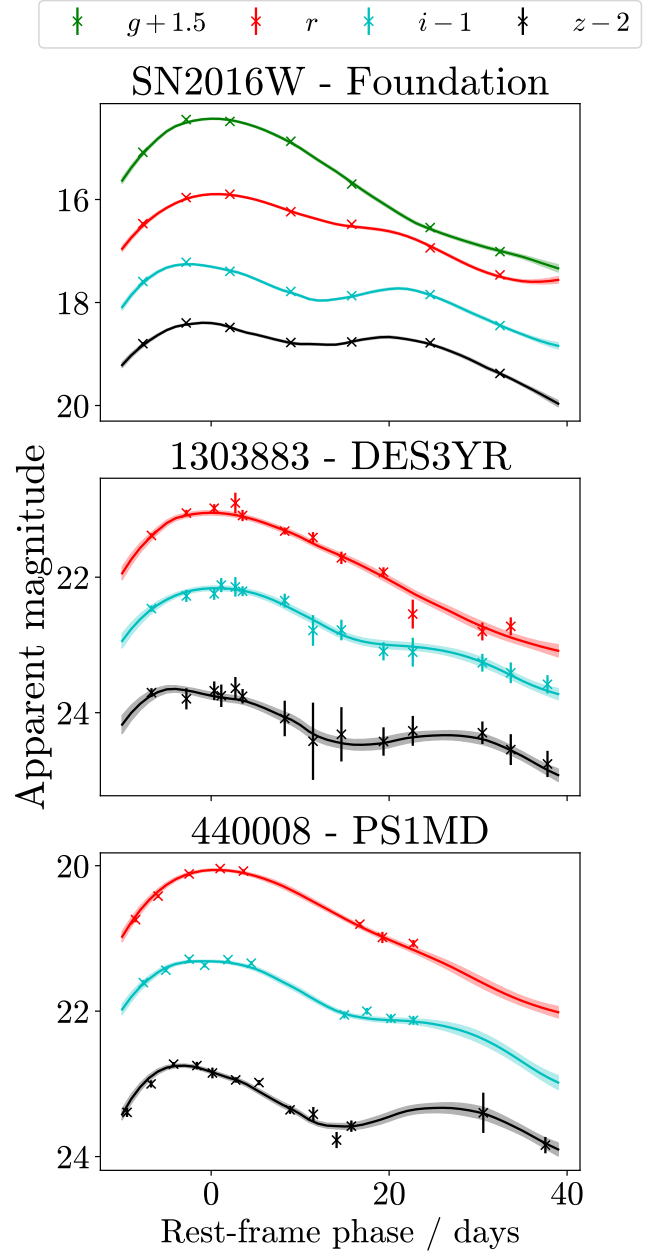


**Figure 2.** Example BayeSN light curve fits to SN2016W from the Foundation sample, 1303883 from the DES3YR sample and 440008 from the PS1MD sample. Bands have been offset arbitrarily for clarity. Note that while the data presented is in magnitude space, all fitting is performed in flux space. Light curves are calculated for all posterior samples of SN latent parameters, and lines and shaded regions represent the mean and standard deviation of all these light curves.

Figure 3, which shows the posteriors for  $\mathbb{E}[R_V]$  and  $\sqrt{\text{Var}[R_V]}$  as well as  $\mu_R$  and  $\sigma_R$  for the PS1MD sample - while the  $\mu_R$  posterior extends all the way to the truncation boundary at 1.2, the posterior on  $\mathbb{E}[R_V]$  shows a clear peak well above 1.2.

Considering  $\sigma_R$  and  $\sqrt{\text{Var}[R_V]}$ , we are able to obtain only upper limits from Foundation and DES3YR; we infer  $\sigma_R = 1.28 \pm 0.41$  and  $\sqrt{\text{Var}[R_V]} = 0.86 \pm 0.23$  from PS1MD. We obtain much greater constraint on  $\sigma_R$  with the combined sample, instead inferring  $\sigma_R = 0.67 \pm 0.27$  and  $\sqrt{\text{Var}[R_V]} = 0.59 \pm 0.20$ .

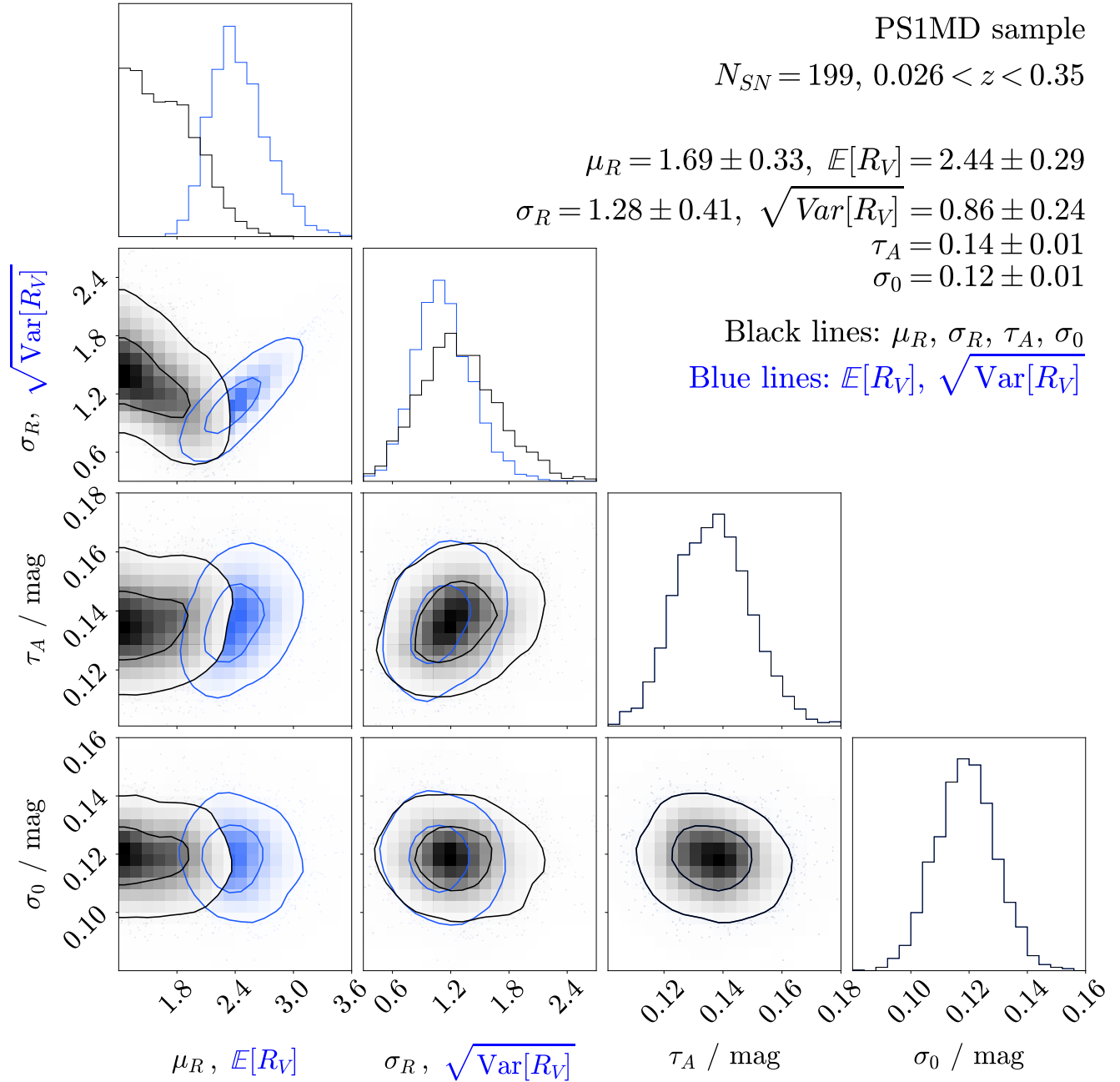


**Figure 3.** Corner plot showing joint and marginal posteriors on  $\mu_R$ ,  $\sigma_R$ ,  $\tau_A$  and  $\sigma_0$  as well as  $\mathbb{E}[R_V]$  and  $\sqrt{\text{Var}[R_V]}$  for the PS1MD sample. This demonstrates the importance of considering  $\mathbb{E}[R_V]$  and  $\sqrt{\text{Var}[R_V]}$  rather than just  $\mu_R$  and  $\sigma_R$  when using truncated distributions.

For  $\tau_A$ , we infer  $0.19 \pm 0.02$  mag,  $0.14 \pm 0.02$  and  $0.14 \pm 0.01$  mag for Foundation, DES3YR and PS1MD respectively. The higher value for Foundation is intriguing; although we have applied redshift cuts to both the DES3YR and PS1MD samples to mitigate for selection effects, it is possible that the sample is lacking higher  $A_V$  objects at higher redshift which is reducing the inferred  $\tau_A$  values for these samples. Nevertheless, all three individual samples are consistent with the combined sample value of  $0.16 \pm 0.01$  mag. Finally, considering  $\sigma_0$  we obtain values of  $0.10 \pm 0.01$ ,  $0.11 \pm 0.01$  and

$0.12 \pm 0.01$  mag for Foundation, DES3YR and PS1MD respectively, and a combined sample value of  $0.11 \pm 0.01$  mag.

It should be noted that our inferred parameters for the SN Ia host galaxy  $R_V$  population distribution are consistent with those from previous hierarchical Bayesian analyses which incorporated both optical and NIR data. Previous analysis using BayeSN in [Thorp & Mandel \(2022\)](#) of 75 nearby SNe from CSP-I ([Krisciunas et al. 2017](#)) found  $\mu_R = 2.59 \pm 0.14$  and  $\sigma_R = 0.62 \pm 0.16$ , while a light curve model-independent analysis of dust reddening based on peak optical and NIR apparent colours of 65 low-redshift SNe Ia presented



**Table 1.** Inferred parameter values when applying our hierarchical dust model to each sub-sample separately, as well as for the combined sample, assuming a truncated normal  $R_V$  distribution.  $\mathbb{E}[R_V]$  and  $\sqrt{\text{Var}[R_V]}$  respectively denote the population mean and square-root of the population variance, as opposed to the fitting parameters  $\mu_R$  and  $\sigma_R$ . Values quoted as  $\mu \pm \sigma$  represent the mean and standard deviation of the posterior, while those quoted as X (Y) denote the 68th (95th) percentiles for parameters where only an upper limit could be constrained.

Sample	$N_{\text{SN}}$	$\mu_R$	$\sigma_R$	$\mathbb{E}[R_V]$	$\sqrt{\text{Var}[R_V]}$	$\tau_A$ / mag	$\sigma_0$ / mag
Foundation	157	2.66±0.13	0.23 (0.47)	2.66±0.13	0.23 (0.47)	0.19±0.02	0.10±0.01
DES3YR	119	3.14±0.59	1.21 (2.93)	3.41±0.57	1.10 (2.04)	0.14±0.02	0.11±0.01
PS1MD	199	1.69±0.33	1.28±0.41	2.44±0.29	0.86±0.23	0.14±0.01	0.12±0.01
Combined	475	2.51±0.15	0.65±0.27	2.58±0.14	0.59±0.20	0.16±0.01	0.11±0.01

in Ward et al. (2023a) found  $\mu_R = 2.61^{+0.38}_{-0.35}$  and placed 68th (95th) percentile upper limits of  $\sigma_R < 0.92(1.96)$ .

## 4.2 Dust Properties Split by Host Mass

We next consider the dust properties binned based on global host galaxy mass. As discussed in Section 3.3.2, we consider three separate variants of this model: an achromatic intrinsic mass step, a difference in baseline intrinsic SED between SNe in high- and low-mass galaxies, and a less flexible model which only incorporates differences in dust properties. The results obtained from these models are summarised in Table 4.2.4, but discussed here in more detail.

### 4.2.1 Intrinsic Achromatic Mass Step

We first consider dust properties under the assumption of an achromatic mass step, with a wavelength-independent intrinsic magnitude offset between SNe in high- and low-mass host galaxies. Figure 4 shows joint and marginal posterior distributions of  $\mathbb{E}[R_V]$ ,  $\sqrt{\text{Var}[R_V]}$ ,  $\tau_A$ ,  $\Delta M_0$  and  $\sigma_0$  for each mass bin (Figure A1 in Appendix A shows the posteriors for the differences in inferred parameter values between each mass bin).

In this case, we find evidence in favour of an intrinsic offset, inferring  $\Delta M_0 = -0.049 \pm 0.016$  at a significance of  $3.1\sigma$ . Moreover, using this model we find no evidence for a difference in  $R_V$  as a function of host galaxy stellar mass; for  $\mathbb{E}[R_V]$  we infer  $2.51 \pm 0.16$  and  $2.74 \pm 0.35$  respectively across high- and low-mass host galaxies, with  $\Delta \mathbb{E}[R_V] = 0.32 \pm 0.58$ , consistent with zero.

In addition to the  $R_V$  distributions and  $\Delta M_0$ , we consider  $\tau_A$  and  $\sigma_0$  separately for high- and low-mass hosts.  $\tau_A$  and  $\Delta M_0$  have similar effects in that increasing both corresponds to a fainter observed SN sample, however the key difference is that  $\Delta M_0$  is achromatic while increasing  $\tau_A$  will also cause the sample to appear redder. We find evidence that  $\tau_A$  is higher for high-mass hosts than low-mass hosts with a difference of  $0.068 \pm 0.018$  mag at a significance of  $\sim 3.7\sigma$ , indicating that there is on average more dust along the line of sight to SNe Ia in high-mass galaxies than low-mass galaxies.

It is noticeable that the posterior distributions for the parameters relating to  $R_V$  are wider for the low-mass bin than for the high-mass bin. In part, this can be simply understood as a consequence of there being more SNe in the high-mass bin. However, we can see from the inferred  $\tau_A$  values that SNe in the high-mass bin have more dust along the line-of-sight on average and therefore provide greater constraint on the properties of the dust.

Finally, concerning  $\sigma_0$  we infer a slightly lower value for high-mass hosts,  $0.10 \pm 0.01$  mag as opposed to  $0.12 \pm 0.01$  mag with a difference of  $-0.031 \pm 0.012$  mag at a significance of  $\sim 2.6\sigma$ .

### 4.2.2 Intrinsic SED Difference

We next consider a more flexible variation of the model, with the baseline ( $\theta_1 = 0$ ) intrinsic SED able to vary between high- and low-mass galaxies. As mentioned previously, any reference to the baseline intrinsic properties refers to the case with  $\theta_1 = 0$ , i.e. independent of light curve stretch.

In this case, the parameters comprising  $\Delta W_0$  are less directly interpretable in a physical sense compared with a specific mass step term  $\Delta M_0$ . However,  $W_0$  corresponds to the baseline intrinsic SED of the SN population; for each posterior sample of  $\Delta W_{0,\text{HM/LM}}$  we can integrate the SED through a given set of passbands in order to calculate intrinsic baseline light and colour curves. In this analysis, we consider derived posterior distributions on mean light and colour curves for SNe in high- and low-mass galaxies separately. We do this comparison by setting  $\theta_1^s = A_V^s = \epsilon^s(\lambda, t) = 0^5$  to assess the baseline dust- and stretch-independent properties of SNe Ia in different environments, after post-processing our MCMC chains to ensure a consistent definition of  $\theta_1$  between high- and low-mass galaxies as discussed in Appendix D.

Figures 5 and 6 respectively show the posterior distributions of baseline dust- and stretch-independent *griz* light curves and *g-r*, *r-i* and *i-z* colour curves for SNe in high- and low-mass galaxies, along with the differences between the two. Figure 7, meanwhile, shows joint and marginal posterior distributions of  $\mathbb{E}[R_V]$ ,  $\sqrt{\text{Var}[R_V]}$ ,  $\tau_A$  and  $\sigma_0$  as well as derived distributions of baseline intrinsic peak *g*-band absolute magnitude and *g-r* colour for each mass bin (Figure A2 in Appendix A shows the posteriors for the differences in inferred parameter values between each mass bin).

Compared with the  $\Delta M_0$  case presented in Section 4.2.1, we are now analysing intrinsic differences as a function of both wavelength and time. Regarding an intrinsic mass step, in the conventional Tripp formula (Tripp 1998) approach for estimating distances to SNe Ia we expect that an intrinsic mass step corresponds to a difference in peak magnitude in some reference band. For this model we will define  $\Delta M_0 = M_{\text{peak,g,HM}}^{\text{int}} - M_{\text{peak,g,LM}}^{\text{int}}$  and infer  $\Delta M_0 = -0.049 \pm 0.027$  mag.

Compared with the achromatic mass step model, we observe a similar magnitude offset but at a lower significance of  $1.8\sigma$ . Of course, in isolation a  $1.8\sigma$  offset is not significant but it is unsurprising that our uncertainties increase when switching to a more flexible model.

Beyond a simple mass step parameter, we should consider how the difference in baseline light and colour curves varies with both time and wavelength. We can consider the intrinsic magnitude difference

<sup>5</sup> In principle,  $\epsilon(\lambda, t)$  has the flexibility to impose differences in the mean colour distribution of SNe in each mass bin independently of  $W_0$ . However, we verify that the posterior samples of  $\epsilon(\lambda, t)$  for both SNe in high- and low-mass galaxies separately do not shift the population mean intrinsic colours.

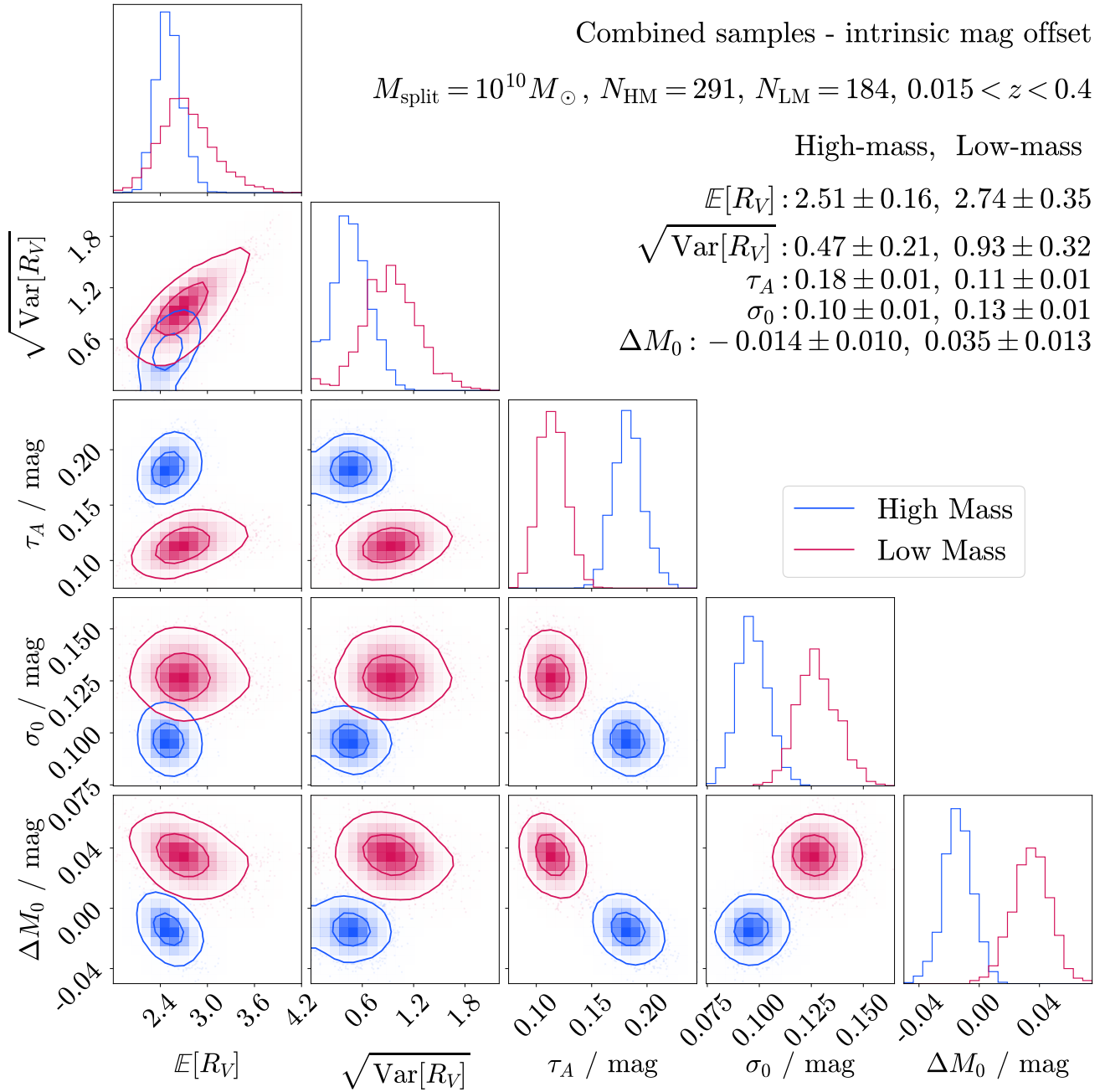


**Figure 4.** Corner plot showing joint and marginal posteriors on  $\mu_R$ ,  $\sigma_R$ ,  $\tau_A$ ,  $\Delta M_0$  and  $\sigma_0$  for high- and low-mass hosts for 475 SNe across Foundation, DES3YR and PS1MD, with the split between high- and low-mass hosts at  $10^{10} M_{\odot}$ . These posteriors are for a model which allows for a constant intrinsic magnitude offset between each mass bin.

at peak in different bands, inferring  $\Delta M_{r,\text{peak}}^{\text{int}} = -0.027 \pm 0.022$ ,  $\Delta M_{i,\text{peak}}^{\text{int}} = -0.032 \pm 0.019$  and  $\Delta M_{z,\text{peak}}^{\text{int}} = -0.016 \pm 0.030$ . The relatively large uncertainties for these values makes it challenging to comment on the wavelength dependence of any magnitude offset at peak. The most significant difference in magnitude is at 20 days post-peak in  $i$ -band, where  $\Delta M_{i,t=20}^{\text{int}} = -0.099 \pm 0.022$  at a significance of  $4.5\sigma$ . Concerning colour, at peak we see a difference in baseline intrinsic  $g-r$  colour between high- and low-mass of  $-0.022 \pm 0.010$  at a significance of  $2.2\sigma$ , weak evidence that SNe Ia in high-mass

galaxies are bluer around peak than those in low-mass galaxies. However, we can also consider other bands and phases; 20 days post-peak, the difference in baseline intrinsic  $r-i$  colour is  $0.067 \pm 0.015$  at a significance of  $4.5\sigma$ . Overall, our results do indicate statistically significant intrinsic differences between SNe Ia in high- and low-mass host galaxies.

In terms of host galaxy dust properties, for the population mean of the  $R_V$  distribution for high-mass bin we infer  $\mathbb{E}[R_V] = 2.26 \pm 0.14$  while for the low mass bin we infer  $\mathbb{E}[R_V] = 3.36 \pm 0.51$ ;

the difference between the values is  $\Delta\mathbb{E}[R_V] = -1.10 \pm 0.53$  at a significance of  $2.1\sigma$ . As in Section 4.2.1, we see a difference in  $\tau_A$  between SNe Ia in high- and low-mass hosts, although this difference is reduced to  $-0.047 \pm 0.024$  mag at a significance of just under  $2\sigma$ . Regarding  $\sigma_0$ , compared with the achromatic mass step model we infer the same value for the high mass bin of  $0.10 \pm 0.01$  mag and a slightly lower value for low-mass galaxies of  $0.12 \pm 0.01$  mag, with the difference between high- and low-mass reduced to  $-0.022 \pm 0.012$  mag.

Beyond considering the posterior distributions of the parameters, we can also compare SNe in high- and low-mass hosts by summarising their physical properties. In Figure 8, we present the mean and standard error on the mean in Hubble residual binned as a function of rest-frame peak  $B - V$  apparent colour (derived from the posterior samples of the latent SN parameters). These values were obtained by fitting the SN sample with the BayeSN model with the values of  $\mu_R$ ,  $\sigma_R$ ,  $\tau_A$ ,  $W_0$ , and  $\sigma_0$  fixed to the medians of the posterior samples for high- and low-mass hosts separately – for these fits, no external distance constraint based on redshift was included. Based on this result, we see no discernible trend between Hubble residual and apparent colour nor a difference in this trend between each bin, although the lack of redder SNe in the low mass bin makes this comparison challenging.

#### 4.2.3 Dust-only Difference

The final case we consider is a model that does not include either of the intrinsic differences assessed previously (or, equivalently, forces these differences to be equal to zero). Under the strong assumption that the SN Ia population is intrinsically identical between high- and low-mass galaxies, for the host galaxy  $R_V$  distribution we infer  $\mathbb{E}[R_V]$  of  $2.39 \pm 0.13$  and  $3.14 \pm 0.39$  for high- and low-mass galaxies respectively, with a difference  $\Delta\mathbb{E}[R_V] = -0.74 \pm 0.41$ . As for the other models which incorporate intrinsic differences, in this case we still infer a difference in  $\tau_A$  between the different mass bins;  $0.18 \pm 0.01$  mag for high-mass and  $0.13 \pm 0.01$  mag for low-mass, with  $\Delta\tau_A = 0.047 \pm 0.017$  mag. There is also a difference in inferred  $\sigma_0$  between the two bins, with  $\Delta\sigma_0 = -0.029 \pm 0.012$  mag in this case.

#### 4.2.4 Discussion

The aim of this binned population analysis is to investigate whether the mass step is driven by intrinsic differences, differences in the host galaxy dust properties or some combination of those two effects. However, before considering the relative contribution of each of these effects we start with a simpler question: are there intrinsic differences between SNe Ia on either side of the mass step?

We have considered two separate model variations which jointly infer intrinsic properties in each bin simultaneously with host galaxy dust properties. The important thing to emphasise is that both of these models are flexible and allow for the possibility of a mass step driven purely by dust; nevertheless, when we condition our models on observed data the inferred parameter values support the existence of non-zero intrinsic differences. When we allow for an intrinsic achromatic magnitude offset between each mass bin, we infer a mass step  $\Delta M_0 = -0.049 \pm 0.016$  mag at a significance of  $3.1\sigma$ . In the more flexible case of a difference in baseline intrinsic SED between mass bins, we infer a similar magnitude offset in  $g$ -band of  $-0.049 \pm 0.027$  mag although at a lower significance of  $1.8\sigma$ , unsurprising given the increased complexity of the model. When looking at intrinsic SED

differences we can additionally examine differences as a function of both wavelength and time. Our analysis shows a difference in intrinsic peak  $g - r$  colour between mass bins of  $2.2\sigma$  significance, providing weak evidence that SNe Ia in high-mass galaxies are intrinsically bluer than their low-mass counterparts in these bands. Looking to other wavelengths and phases, we also find much more significant differences. For example, 20 days post-peak we find that there are differences in baseline intrinsic  $i$ -band magnitude and  $r - i$  colour of  $4.5\sigma$  significance. Overall, our results do support the existence of intrinsic differences.

Brout & Scolnic (2021); Popovic et al. (2023) posit that the mass step is driven solely by differences in dust properties between high- and low-mass galaxies. Our analysis, however, does find significant intrinsic differences and therefore contradicts this idea. Our results also differ from those of Karchev et al. (2023a), which disfavours both intrinsic and extrinsic differences between SNe Ia in different mass bins. We note that the main difference between our approach and that of Karchev et al. (2023a) is that we have also treated the population mean  $V$ -band extinction ( $\tau_A$ ) as a separate parameter for each mass bin. We next consider what our results can tell us about the relative contributions of intrinsic and extrinsic effects in driving the mass step.

As part of our analysis, we do consider a model which assumes no intrinsic differences between mass bins and only allows the dust properties to vary. We find a lower population mean  $R_V$  of  $\mathbb{E}[R_V] = 2.39 \pm 0.13$  for SNe Ia in high-mass galaxies compared with low-mass galaxies, for which we infer  $\mathbb{E}[R_V] = 3.14 \pm 0.39$ . This is similar to the trend found in Brout & Scolnic (2021); Popovic et al. (2023). In this case, it is not surprising that we infer differences in the host galaxy dust properties; by definition, differences in dust properties were the only effect included in the model which were allowed to explain the mass step.

When we increase the flexibility of our model to jointly infer an achromatic magnitude offset between mass bins alongside dust properties, our results no longer provide any evidence to support a difference in  $R_V$  distribution; for high- and low-mass bins respectively, we infer  $2.51 \pm 0.16$  and  $2.74 \pm 0.35$  for  $\mathbb{E}[R_V]$ . When we allow for a magnitude offset, our results support the idea of a mass step driven solely by intrinsic differences. However, while this model is more flexible than the previous case it still carries the assumption that the baseline intrinsic colours of SNe Ia in each mass bin are identical, only allowing for a magnitude shift.

For the final case, which allows for both time and wavelength-dependent differences in the baseline intrinsic SED between each mass bin, we infer  $\mathbb{E}[R_V]$  values of  $2.26 \pm 0.14$  and  $3.36 \pm 0.51$  for high- and low-mass bins respectively. The difference between these two values is  $\Delta\mathbb{E}[R_V] = -1.10 \pm 0.53$  at a significance of  $2.1\sigma$ . Our interpretation of these results is somewhat limited by the weak constraint we are able to place on  $\mathbb{E}[R_V]$  for the low-mass bin, given the lower overall extinction of SNe Ia in this bin. Considering Hubble residuals and apparent peak  $B - V$  colours, we see no evidence for a relation between the two nor any difference in this relation between each mass bin. However, this analysis is again limited by the lack of redder SNe in the low-mass bin. Our results do not provide strong evidence in favour of a mass step driven in part by extrinsic differences, but nor can we rule it out.

The flexible model we have used, equitably treating differences in the intrinsic baseline SED of SNe Ia in each mass bin alongside differences in dust properties, has a number of advantages. However, the complexity of the effects described by the model and their relative interplay makes this a challenging problem to solve. We observe intrinsic differences in peak  $g$ -band magnitude and  $g - r$  colour

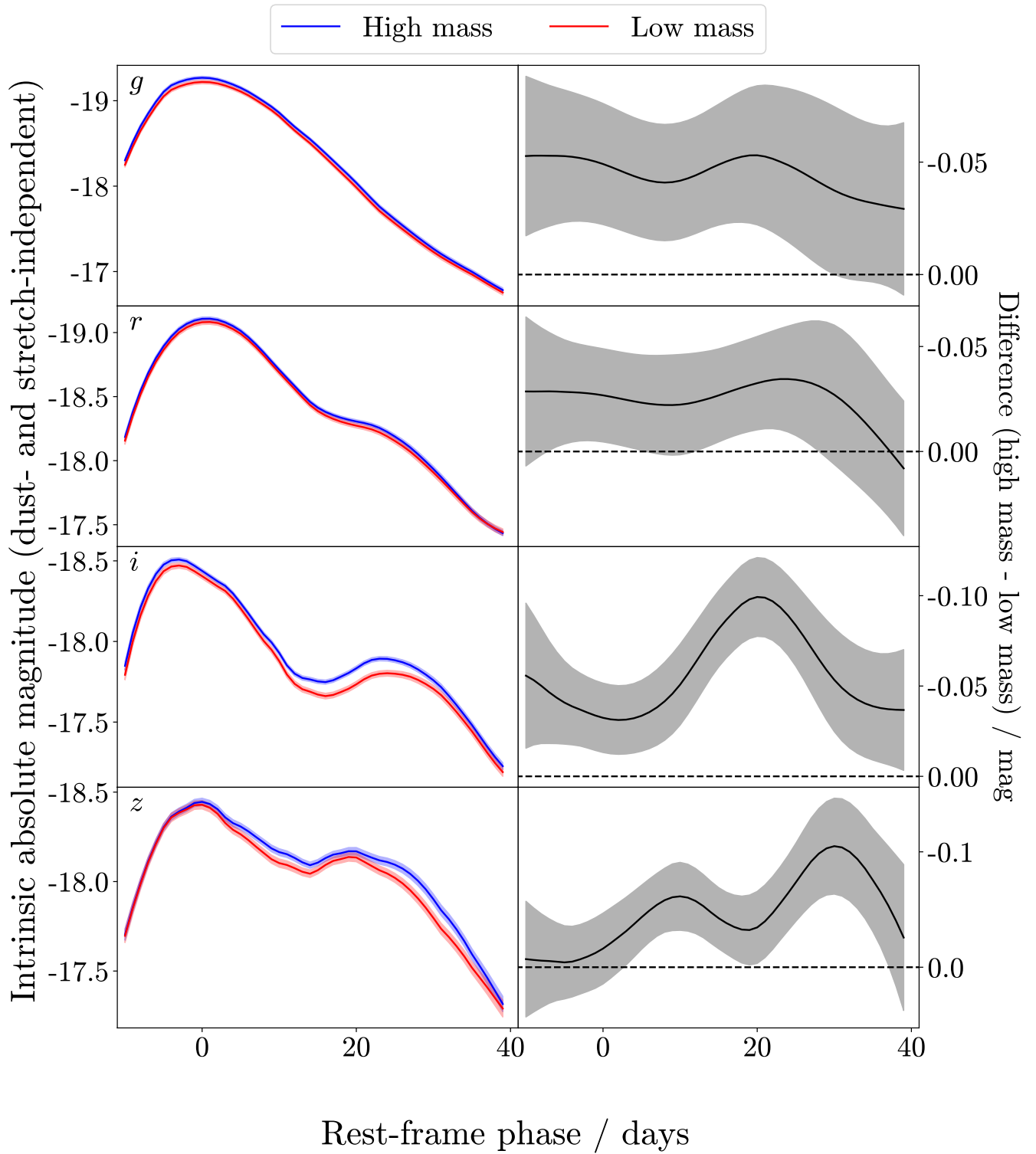


**Figure 5.** **Left panels:** Posterior inference of the baseline dust- and stretch-independent intrinsic absolute SN Ia light curve in each of the *griz* bands, evaluated from the posterior samples of  $W_{0, \text{HM/LM}}$ . Solid lines and shaded regions represent the posterior mean and standard deviation (uncertainty) of the baseline light curve in each mass bin and band. **Right panels:** Posterior inference of the difference between baseline light curves depicted in left panels. Solid lines and shaded regions again represent the posterior mean and standard deviation (uncertainty) of the difference.

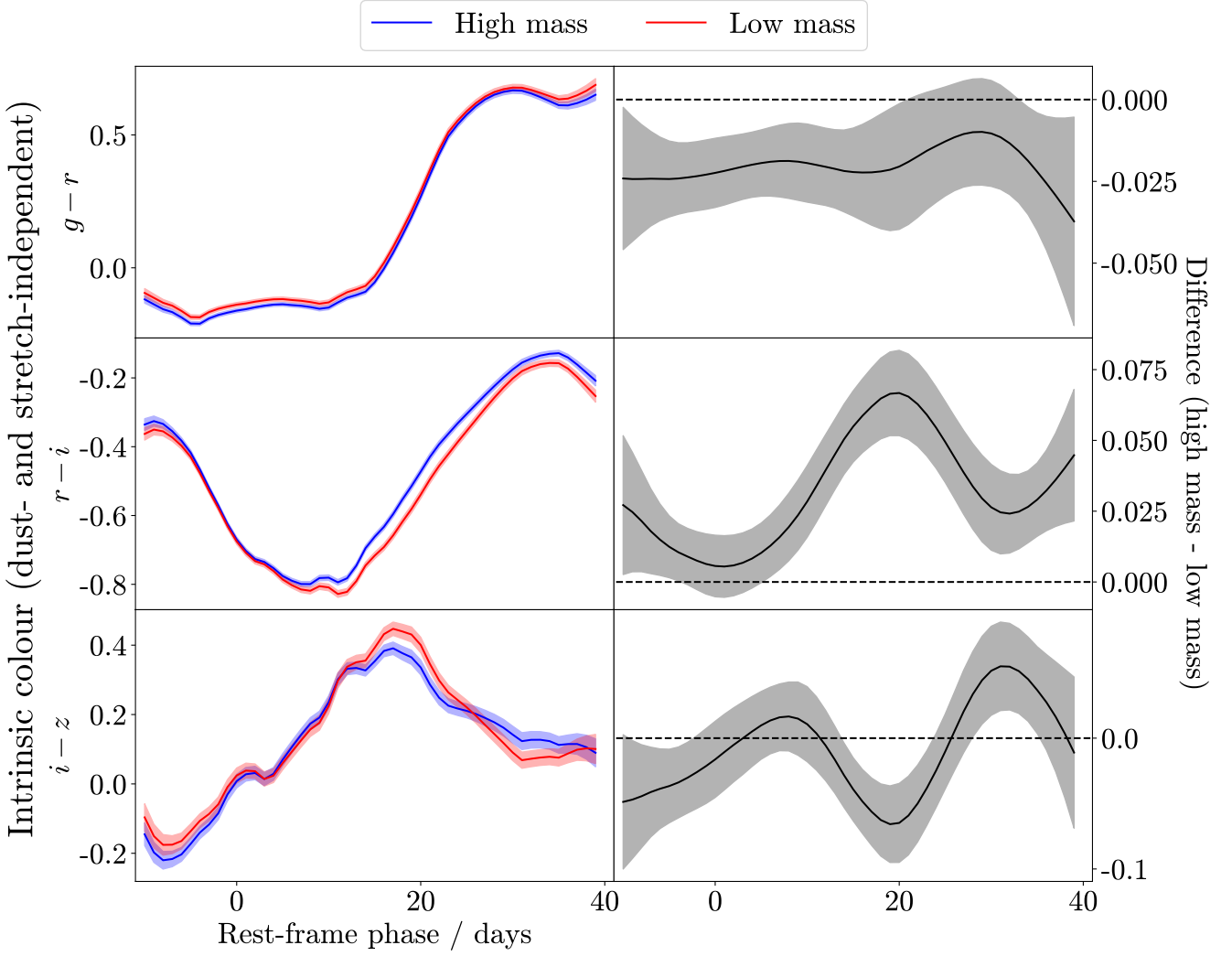


**Figure 6.** Posterior inference of the baseline dust- and stretch-independent intrinsic SN Ia colour curve for  $g-r$ ,  $r-i$  and  $i-z$  colours, evaluated from the posterior samples of  $W_{0, \text{HM/LM}}$ . Solid lines and shaded regions represent the posterior mean and standard deviation (uncertainty) of the baseline colour curve in each mass bin and band. **Right panels:** Posterior inference of the difference between baseline intrinsic colour curves depicted in left panels. Solid lines and shaded regions again represent the posterior mean and standard deviation (uncertainty) of the difference.

with significances of  $1.8\text{--}2.2\sigma$  (albeit with intrinsic differences of  $4.5\sigma$  at other phases), as well as a difference in  $\Delta\mathbb{E}[R_V]$  with  $2.1\sigma$  significance. The combined sample of 475 SNe Ia used in this work has provided evidence in favour of intrinsic differences between SNe Ia in different mass bins, but further analysis of larger samples is necessary to allow for more confident conclusions about the relative contributions of intrinsic and extrinsic effects in explaining the mass step.

Within this work, we have focused on SN Ia properties split based on their host galaxy stellar mass. However, as mentioned in Section 1 previous work has established relations between SN Ia luminosity and other galaxy properties besides stellar mass, for example SFR, sSFR and rest-frame colour. These relations are also stronger when considering the properties of the local environment in which the SN exploded rather than global properties of the entire host galaxy.

The BayeSN model we have used for this work can be modified to incorporate population splits on other parameters, and future studies can analyse intrinsic and extrinsic differences as a function of any host property using our approach.

### 4.3 Redshift Evolution

We next consider the possibility of a dust distribution which varies as a function of redshift, using the linear model as outlined in Section 3.3.3. The results of this analysis are shown in Table 3.

For the gradient of the  $\tau_A$  redshift relation, we infer  $\eta_\tau = -0.22 \pm 0.06$  mag, non-zero at  $\sim 3.7\sigma$  significance. A challenge in interpreting this result is that Malmquist bias would be expected to lead to smaller inferred values of  $\tau_A$  at higher redshift. While we have mitigated for this by applying selection effects to the DES3YR

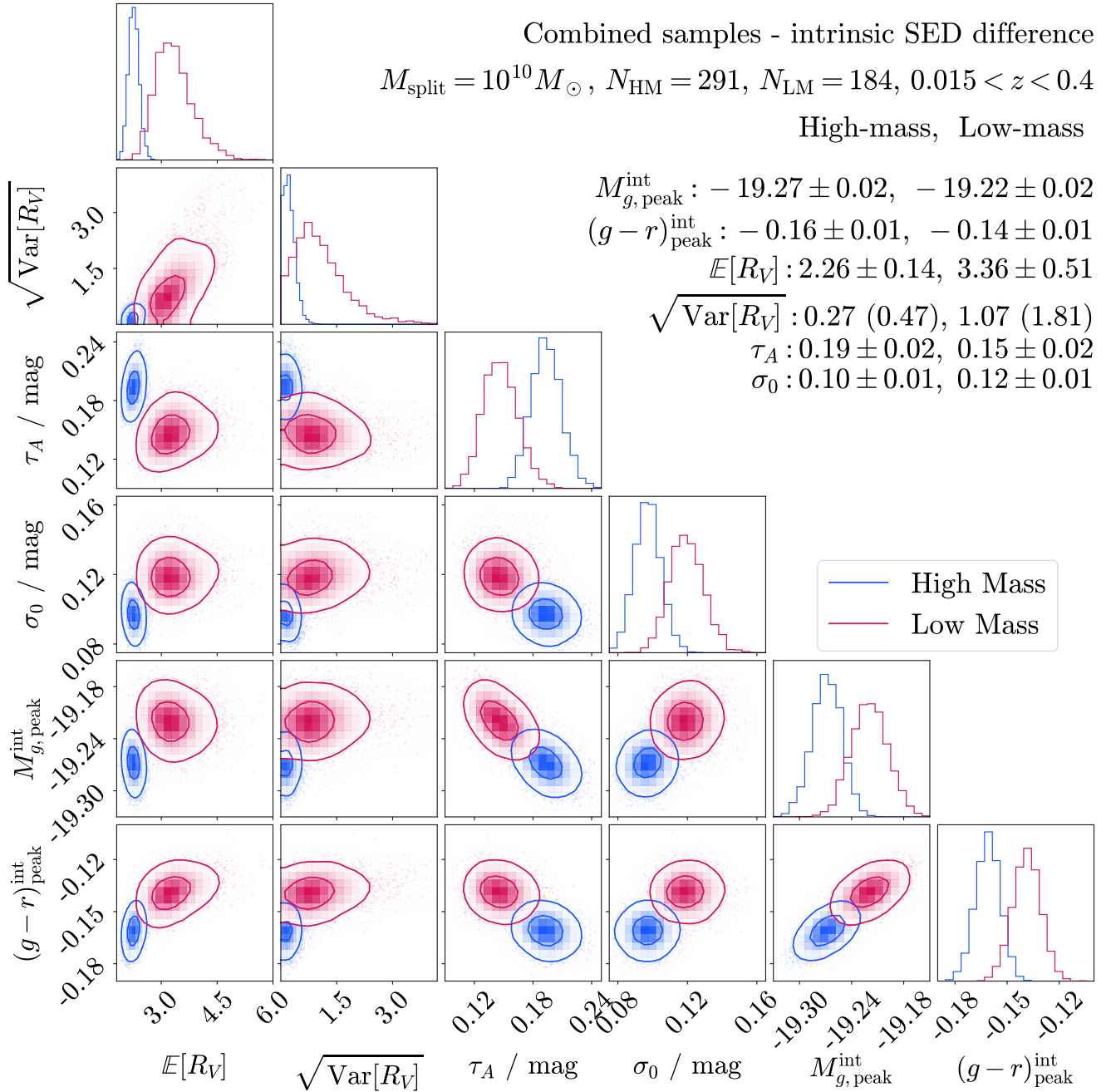


**Figure 7.** Corner plot showing joint and marginal posteriors on  $\mathbb{E}[R_V]$ ,  $\sqrt{\text{Var}[R_V]}$ ,  $\tau_A$  and  $\sigma_0$ , as well as derived baseline intrinsic peak  $g$ -band absolute magnitude and  $g-r$  colour, for high- and low-mass hosts for 475 SNe across Foundation, DES3YR and PS1MD. This model allows for a difference in baseline intrinsic SED between each mass bin.

and PS1MD samples, some small effect may remain - overall, we caution that this result should be interpreted as an evolution in the effective  $\tau_A$  in the samples we are looking at with redshift, rather than necessarily a physical evolution with redshift in the distribution of  $A_V$ . Nevertheless, it is important that  $\tau_A$  is free to evolve with redshift in the model in order to fairly assess any evolution with redshift of  $\mu_R$ .

Considering the  $R_V$  distribution itself, our results do not provide any evidence that it evolves with redshift across the Foundation,

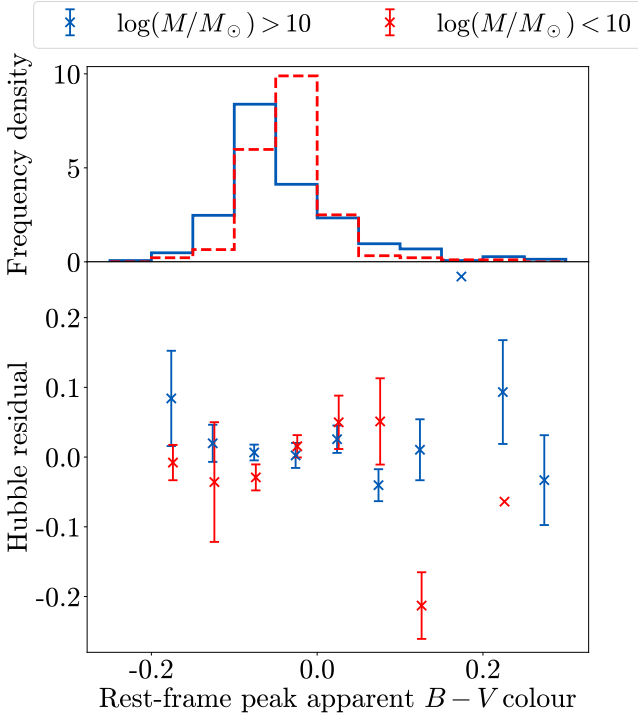
DES3YR and PS1MD samples - we find the gradient of the  $\mu_R$ -redshift relation to be  $\eta_R = -0.38 \pm 0.70$ , consistent with zero. While we have performed this analysis with  $\tau_A$  also free to evolve with redshift, it should be noted that our conclusions are unchanged when we fix  $\tau_A$  to be constant with redshift. However, we emphasise that the samples included in this work are all below  $z = 0.4$  and that further analyses with higher redshift objects are required to investigate the possibility of redshift evolution further.

**Table 2.** Inferred parameter values for our hierarchical dust model with separate population parameters for SNe in host galaxies above and below  $10^{10}M_{\odot}$  for the combined sample of 475 SNe Ia. We present results for cases allowing for an intrinsic magnitude difference between bins, an intrinsic SED difference and no intrinsic difference. In some cases,  $\Delta$  values are presented which correspond to the difference between posterior samples for SNe in high-mass hosts and low-mass hosts.

Method	$\Delta M_0 / \text{mag}$	$\Delta(g-r)_{\text{peak}}^{\text{int}}$	$\mathbb{E}[R_V]$		$\sqrt{\text{Var}[R_V]}$		...
			HM	LM	HM	LM	
Intrinsic mag diff.	$-0.049 \pm 0.016$	–	$2.51 \pm 0.16$	$2.74 \pm 0.35$	$0.47 \pm 0.21$	$0.93 \pm 0.32$	
Intrinsic SED diff.	$-0.049 \pm 0.027$	$-0.022 \pm 0.010$	$2.26 \pm 0.14$	$3.36 \pm 0.51$	$0.27 (0.49)$	$1.07 (1.81)$	
No intrinsic diff.	–	–	$2.39 \pm 0.13$	$3.14 \pm 0.39$	$0.43 \pm 0.20$	$1.09 \pm 0.43$	

...	$\tau_A / \text{mag}$		$\sigma_0 / \text{mag}$		$\Delta \mathbb{E}[R_V]$	$\Delta \sqrt{\text{Var}[R_V]}$	$\Delta \tau_A / \text{mag}$	$\Delta \sigma_0 / \text{mag}$
	HM	LM	HM	LM				
	$0.18 \pm 0.01$	$0.11 \pm 0.01$	$0.10 \pm 0.01$	$0.13 \pm 0.01$	$-0.23 \pm 0.38$	$-0.47 \pm 0.38$	$0.068 \pm 0.018$	$-0.031 \pm 0.012$
	$0.19 \pm 0.02$	$0.15 \pm 0.02$	$0.10 \pm 0.01$	$0.12 \pm 0.01$	$-1.10 \pm 0.53$	$-0.69 \pm 0.53$	$0.047 \pm 0.024$	$-0.022 \pm 0.012$
	$0.18 \pm 0.01$	$0.13 \pm 0.01$	$0.10 \pm 0.01$	$0.13 \pm 0.01$	$-0.74 \pm 0.41$	$-0.66 \pm 0.48$	$0.047 \pm 0.017$	$-0.029 \pm 0.012$



**Figure 8. Upper panel:** Distributions of rest-frame apparent  $B - V$  colour at peak in both high and low-mass bins. **Lower panel:** Binned Hubble residual mean and standard error on the mean obtained from fitting SNe in high- and low-mass hosts with the BayeSN model, based on the population parameters inferred when treating these samples separately, binned as a function of rest-frame apparent  $B - V$  colour at peak. Bins are from  $-0.25$  to  $0.25$  with widths of  $0.05$  – note that the binning used was identical for high- and low-mass hosts and the bins are offset slightly for clarity. Please note that we have restricted the y-axis range for presentation purposes; there are two data points that lie outside this range which are for bins containing single objects that have large Hubble residuals.

## 5 CONCLUSIONS AND FUTURE WORK

In this work we apply BayeSN, a hierarchical Bayesian SED model for SNe Ia, to infer the global dust distributions for samples from Foundation, DES3YR and PS1MD. We have investigated the possibility

**Table 3.** Inferred parameter values for our hierarchical dust model which allows  $\mu_R$  and  $\tau_A$  to vary with redshift.

Parameter	Value
$\mu_{R,z0}$	$2.58 \pm 0.17$
$\eta_R$	$-0.38 \pm 0.70$
$\tau_{A,z0} / \text{mag}$	$0.19 \pm 0.02$
$\eta_{\tau} / \text{mag}$	$-0.22 \pm 0.06$
$\sigma_R$	$0.61 \pm 0.24$
$\sigma_0 / \text{mag}$	$0.11 \pm 0.01$

that the host galaxy mass step can be explained solely by differences in the dust population between high- and low-mass galaxies, and also perform the first hierarchical analysis allowing for a redshift evolution in the dust population. Our findings can be summarised as follows:

- For a combined sample of 475 SNe Ia from Foundation, DES3YR and PS1MD (with redshift cuts applied to mitigate for selection effects), we infer the population mean of the line-of-sight  $R_V$  distribution to be  $\mathbb{E}[R_V] = 2.58 \pm 0.14$ , the square root of the  $R_V$  population variance to be  $\sqrt{\text{Var}[R_V]} = 0.59 \pm 0.20$ , the population mean  $A_V$  to be  $\tau_A = 0.16 \pm 0.01$  mag and the intrinsic dispersion to be  $\sigma_0 = 0.11 \pm 0.01$  mag. Considering each sub-sample separately, we infer values consistent with these.

- When jointly inferring differences in intrinsic properties simultaneously with differences in host galaxy properties, we find evidence for intrinsic differences between SNe in host galaxies with stellar masses above and below  $10^{10}M_{\odot}$ . Allowing for a constant, achromatic magnitude offset between each mass bin, we infer an intrinsic mass step of  $-0.049 \pm 0.016$  mag and no evidence for any difference in the  $R_V$  distributions. However, we also apply a more flexible model which allows for time- and wavelength-dependent differences in the intrinsic SED between the two populations. In this case, we infer differences in peak stretch and dust-independent intrinsic  $g$ -band magnitude and  $g - r$  colour of  $-0.049 \pm 0.027$  and  $-0.022 \pm 0.010$ , and more significant differences in intrinsic  $i$ -band magnitude and  $r - i$  colour 20 days after peak of  $-0.099 \pm 0.022$  and  $0.067 \pm 0.015$ . For this model we also infer a difference in the population mean of the  $R_V$  distribution for each mass bin of  $\Delta \mathbb{E}[R_V] = -1.10 \pm 0.53$ . These results suggest that extrinsic effects, in addition to intrinsic effects, may contribute to the host galaxy mass step. Future analyses of this

type on larger samples will allow for better constraints of each of these effects to better understand their relative contributions.

- Across all model variants we infer consistently larger line-of-sight population mean  $A_V$  ( $\tau_A$ ) values for SNe Ia in high-mass galaxies than for SNe Ia in low-mass galaxies. When allowing for a constant intrinsic magnitude offset between each mass bin we infer a difference of  $\Delta\tau_A = 0.068 \pm 0.018$  mag, although this is reduced to  $\Delta\tau_A = 0.047 \pm 0.024$  mag when allowing the baseline, stretch-independent intrinsic SED to vary with both time and wavelength between each mass bin.

- We apply a model which allows  $\mu_R$  and  $\tau_A$  to vary with redshift, modelling these relations as a straight line and constraining both the value at  $z = 0$  and the gradient of the relation with redshift ( $\eta_R$  and  $\eta_\tau$ ). We find no evidence that  $\mu_R$  evolves with redshift over the range covered by the samples used for this work, inferring  $\eta_R = -0.38 \pm 0.70$ , consistent with 0. Concerning  $\tau_A$ , we infer  $\eta_\tau = -0.22 \pm 0.06$  mag, however we emphasise that some small selection effects may remain in spite of our redshift cuts and that this result should be interpreted as an evolution in the effective  $\tau_A$  in these samples rather than necessarily suggesting a physical evolution with redshift in the distribution of  $A_V$ . Future studies involving higher redshift objects should investigate this further.

Our flexible BayeSN, SED-based approach to studying intrinsic and extrinsic properties of SNe Ia provides an ideal framework for studying how the population varies with different host galaxy properties. As discussed in Section 3.1, this analysis was performed using a new, GPU-accelerated implementation of BayeSN; this code has improved performance by a factor of  $\sim 100$ , making it suitable for application to large SN samples, and is made publicly available. Further performance increases (up to an additional factor of  $\sim 10$ ) are possible through the use of Variational Inference (VI; Blei et al. 2016), which is planned for inclusion within BayeSN (Uzsoy 2022).

Alternatively, it is also possible to use the BayeSN model in an SBI framework. Karchev et al. (to be submitted) presents dust inference using BayeSN with truncated marginal neural ratio estimation (TM-NRE; Miller et al. 2021 for the method itself, Karchev et al. 2023b for a specific application to SN cosmology), an SBI approach which uses neural networks to derive posterior distributions where an analytic likelihood is not possible. Such an approach has the potential to fully incorporate survey selection effects – which can be simulated but not expressed analytically – within the hierarchical framework rather than requiring a redshift cut as we have used for this analysis.

In this work, we have focused on physical properties of the population of SNe Ia, conditioned on a fixed cosmology. However, the BayeSN code we make available can also be used to infer cosmology-independent distances whilst marginalising over the intrinsic and extrinsic variations in the population, and is being integrated within SNANA. Additionally, the SBI approach to dust inference using BayeSN presented in Karchev et al. (to be submitted) provides a path towards a fully hierarchical cosmological analysis of SNe Ia all the way from light curves to cosmological parameters, taking survey selection effects into account. Moving forward, BayeSN can therefore be a key component of cosmological analyses.

## ACKNOWLEDGEMENTS

MG and KSM are supported by the European Union’s Horizon 2020 research and innovation programme under ERC Grant Agreement No. 101002652 and Marie Skłodowska-Curie Grant Agreement No. 873089. ST was supported by the European Research Council (ERC) under the European Union’s Horizon 2020 research and innovation

programme (grant agreement no. 101018897 CosmicExplorer). SD acknowledges support from the Marie Curie Individual Fellowship under grant ID 890695 and a Junior Research Fellowship at Lucy Cavendish College. BMB is supported by the Cambridge Centre for Doctoral Training in Data-Intensive Science funded by the UK Science and Technology Facilities Council (STFC). EEH is supported by a Gates Cambridge Scholarship (#OPP1144). SMW is supported by the UK Science and Technology Facilities Council (STFC).

This work was performed using resources provided by the Cambridge Service for Data Driven Discovery (CSD3) operated by the University of Cambridge Research Computing Service ([www.csd3.cam.ac.uk](http://www.csd3.cam.ac.uk)), provided by Dell EMC and Intel using Tier-2 funding from the Engineering and Physical Sciences Research Council (capital grant EP/T022159/1), and DiRAC funding from the Science and Technology Facilities Council ([www.dirac.ac.uk](http://www.dirac.ac.uk)).

## DATA AVAILABILITY STATEMENT

The data underlying this article are sourced from the Pantheon+ compilation of SNe Ia (Scolnic et al. 2022), available at <https://github.com/PantheonPlusSH0ES/DataRelease>. The code used for this analysis is available at <https://github.com/bayesn/bayesn>.

## REFERENCES

- Aleo P. D., et al., 2023, *ApJS*, 266, 9  
 Astier P., et al., 2006, *A&A*, 447, 31  
 Bellm E. C., et al., 2019a, *PASP*, 131, 018002  
 Bellm E. C., et al., 2019b, *PASP*, 131, 068003  
 Betancourt M., 2017, preprint, ([arXiv:1701.02434](https://arxiv.org/abs/1701.02434))  
 Betancourt M. J., Byrne S., Girolami M., 2014, preprint, ([arXiv:1411.6669](https://arxiv.org/abs/1411.6669))  
 Betoule M., et al., 2014, *A&A*, 568, A22  
 Bingham E., et al., 2019, *J. Machine Learning Res.*, 20, 1  
 Blei D. M., Kucukelbir A., McAuliffe J. D., 2016, preprint, ([arXiv:1601.00670](https://arxiv.org/abs/1601.00670))  
 Bradbury J., et al., 2018, JAX: composable transformations of Python+NumPy programs. <http://github.com/google/jax>  
 Briday M., et al., 2022, *A&A*, 657, A22  
 Brout D., Scolnic D., 2021, *ApJ*, 909, 26  
 Brout D., et al., 2019, *ApJ*, 874, 150  
 Brout D., et al., 2022, *ApJ*, 938, 110  
 Burkard J., 2014. Department of Scientific Computing Website, Florida State University, Tallahassee  
 Burns C. R., et al., 2011, *AJ*, 141, 19  
 Burns C. R., et al., 2014, *ApJ*, 789, 32  
 Carpenter B., et al., 2017, *J. Statistical Software*, 76, 1  
 Carrick J., Turnbull S. J., Lavaux G., Hudson M. J., 2015, *MNRAS*, 450, 317  
 Childress M., et al., 2013, *ApJ*, 770, 108  
 Childress M. J., Wolf C., Zahid H. J., 2014, *MNRAS*, 445, 1898  
 Contreras C., et al., 2010, *AJ*, 139, 519  
 Dark Energy Survey Collaboration et al., 2016, *MNRAS*, 460, 1270  
 Dark Energy Survey Collaboration et al., 2024, preprint ([arXiv:2401.02929](https://arxiv.org/abs/2401.02929))  
 Dhawan S., Thorp S., Mandel K. S., Ward S. M., Narayan G., Jha S. W., Chant T., 2023, *MNRAS*, 524, 235  
 Draine B. T., 2003, *ARA&A*, 41, 241  
 Duarte J., et al., 2023, *A&A*, 680, A56  
 Fitzpatrick E. L., 1999, *PASP*, 111, 63  
 Foley R. J., et al., 2018, *MNRAS*, 475, 193  
 Frieman J. A., et al., 2008, *AJ*, 135, 338  
 Gelman A., Rubin D. B., 1992, *Statistical Sci.*, 7, 457



- González-Gaitán S., de Jaeger T., Galbany L., Mourão A., Paulino-Afonso A., Filippenko A. V., 2021, *MNRAS*, **508**, 4656
- Gupta R. R., et al., 2011, *ApJ*, **740**, 92
- Guy J., et al., 2007, *A&A*, **466**, 11
- Hicken M., et al., 2009, *ApJ*, **700**, 331
- Hicken M., et al., 2012, *ApJS*, **200**, 12
- Hoffman M. D., Gelman A., 2014, *J. Machine Learning Res.*, **15**, 1593
- Hsiao E. Y., Conley A., Howell D. A., Sullivan M., Pritchett C. J., Carlberg R. G., Nugent P. E., Phillips M. M., 2007, *ApJ*, **663**, 1187
- Ivezic Ž., et al., 2019, *ApJ*, **873**, 111
- Johansson J., et al., 2021, *ApJ*, **923**, 237
- Jones D. O., Riess A. G., Scolnic D. M., 2015, *ApJ*, **812**, 31
- Jones D. O., et al., 2018, *ApJ*, **867**, 108
- Jones D. O., et al., 2019, *ApJ*, **881**, 19
- Jones D. O., et al., 2021, *ApJ*, **908**, 143
- Jones D. O., et al., 2022, *ApJ*, **933**, 172
- Jones D. O., Kenworthy W. D., Dai M., Foley R. J., Kessler R., Pierel J. D. R., Siebert M. R., 2023, *ApJ*, **951**, 22
- Kaiser N., et al., 2010, in Stepp L. M., Gilmozzi R., Hall H. J., eds, *Society of Photo-Optical Instrumentation Engineers (SPIE) Conference Series Vol. 7733, Ground-based and Airborne Telescopes III*. p. 77330E, doi:10.1117/12.859188
- Karcev K., Trotta R., Weniger C., 2023a, *arXiv e-prints*, p. arXiv:2311.15650
- Karcev K., Trotta R., Weniger C., 2023b, *MNRAS*, **520**, 1056
- Kelly P. L., Hicken M., Burke D. L., Mandel K. S., Kirshner R. P., 2010, *ApJ*, **715**, 743
- Kelsey L., et al., 2021, *MNRAS*, **501**, 4861
- Kenworthy W. D., et al., 2021, *ApJ*, **923**, 265
- Kessler R., et al., 2009, *PASP*, **121**, 1028
- Kim Y.-L., Smith M., Sullivan M., Lee Y.-W., 2018, *ApJ*, **854**, 24
- Kim Y.-L., Kang Y., Lee Y.-W., 2019, *J. Korean Astron. Soc.*, **52**, 181
- Krisciunas K., et al., 2017, *AJ*, **154**, 211
- Lampeitl H., et al., 2010, *ApJ*, **722**, 566
- Maguire K., 2017, in Alsabti A. W., Murdin P., eds, *Handbook of Supernovae*. Springer Cham, p. 293, doi:10.1007/978-3-319-21846-5\_36
- Malmquist K. G., 1922, *Medd. från Lunds Astron. Observ. Serie I*, **100**, 1
- Mandel K. S., Wood-Vasey W. M., Friedman A. S., Kirshner R. P., 2009, *ApJ*, **704**, 629
- Mandel K. S., Narayan G., Kirshner R. P., 2011, *ApJ*, **731**, 120
- Mandel K. S., Scolnic D. M., Shariff H., Foley R. J., Kirshner R. P., 2017, *ApJ*, **842**, 93
- Mandel K. S., Thorp S., Narayan G., Friedman A. S., Avelino A., 2022, *MNRAS*, **510**, 3939
- Meldorf C., et al., 2023, *MNRAS*, **518**, 1985
- Miller B. K., Cole A., Forré P., Louppe G., Weniger C., 2021, in *Advances in Neural Information Processing Systems*. Curran Associates, Inc., pp 129–143, <https://proceedings.neurips.cc/paper/2021/hash/01632f7b7a127233fa1188bd6c2e42e1-Abstract.html>
- Moreno-Raya M. E., López-Sánchez Á. R., Mollá M., Galbany L., Vílchez J. M., Carnero A., 2016a, *MNRAS*, **462**, 1281
- Moreno-Raya M. E., Mollá M., López-Sánchez Á. R., Galbany L., Vílchez J. M., Carnero Rosell A., Domínguez I., 2016b, *ApJ*, **818**, L19
- Neal R., 2011, in Brooks S., Gelman A., Jones G., Meng X.-L., eds, *Handbook of Markov Chain Monte Carlo*. Chapman & Hall/CRC, pp 113–162, doi:10.1201/b10905
- Perlmutter S., et al., 1999, *ApJ*, **517**, 565
- Phan D., Pradhan N., Jankowiak M., 2019, preprint, (arXiv:1912.11554)
- Phillips M. M., 1993, *ApJ*, **413**, L105
- Phillips M. M., et al., 2019, *PASP*, **131**, 014001
- Planck Collaboration et al., 2020, *A&A*, **641**, A6
- Ponder K. A., Wood-Vasey W. M., Weyant A., Barton N. T., Galbany L., Liu S., Garnavich P., Matheson T., 2021, *ApJ*, **923**, 197
- Popovic B., Brout D., Kessler R., Scolnic D., Lu L., 2021, *ApJ*, **913**, 49
- Popovic B., Brout D., Kessler R., Scolnic D., 2023, *ApJ*, **945**, 84
- Rest A., et al., 2014, *ApJ*, **795**, 44
- Riess A. G., et al., 1998, *AJ*, **116**, 1009
- Riess A. G., et al., 2022, *ApJ*, **934**, L7
- Rigault M., et al., 2013, *A&A*, **560**, A66
- Rigault M., et al., 2015, *ApJ*, **802**, 20
- Rigault M., et al., 2020, *A&A*, **644**, A176
- Roman M., et al., 2018, *A&A*, **615**, A68
- Rose B. M., Garnavich P. M., Berg M. A., 2019, *ApJ*, **874**, 32
- Sako M., et al., 2011, *ApJ*, **738**, 162
- Sako M., et al., 2018, *PASP*, **130**, 064002
- Schlafly E. F., Finkbeiner D. P., 2011, *ApJ*, **737**, 103
- Scolnic D. M., et al., 2018, *ApJ*, **859**, 101
- Scolnic D., et al., 2022, *ApJ*, **938**, 113
- Smith M., et al., 2020, *MNRAS*, **494**, 4426
- Stan Development Team 2023, *Stan Modelling Language Users Guide and Reference Manual v.2.33*. <https://mc-stan.org>
- Stritzinger M. D., et al., 2011, *AJ*, **142**, 156
- Sullivan M., et al., 2010, *MNRAS*, **406**, 782
- Thorp S., Mandel K. S., 2022, *MNRAS*, **517**, 2360
- Thorp S., Mandel K. S., Jones D. O., Ward S. M., Narayan G., 2021, *MNRAS*, **508**, 4310
- Tripp R., 1998, *A&A*, **331**, 815
- Uddin S. A., et al., 2020, *ApJ*, **901**, 143
- Uddin S. A., et al., 2023, preprint, (arXiv:2308.01875)
- Uzsoy A. S., 2022, Master's thesis, Univ. Cambridge, [https://www.mlmi.eng.cam.ac.uk/files/2021-2022\\_dissertations/scalable\\_bayesian\\_inference\\_for\\_probabilistic\\_spectrotemporal\\_models.pdf](https://www.mlmi.eng.cam.ac.uk/files/2021-2022_dissertations/scalable_bayesian_inference_for_probabilistic_spectrotemporal_models.pdf)
- Vehtari A., Gelman A., Simpson D., Carpenter B., Bürkner P.-C., 2021, *Bayesian Analysis*, **16**, 667
- Vincenzi M., et al., 2024, preprint (arXiv:2401.02945)
- Ward S. M., Dhawan S., Mandel K. S., Grayling M., Thorp S., 2023a, *MNRAS*, **526**, 5715
- Ward S. M., et al., 2023b, *ApJ*, **956**, 111
- Wiseman P., et al., 2020, *MNRAS*, **495**, 4040
- Wiseman P., Sullivan M., Smith M., Popovic B., 2023, *MNRAS*, **520**, 6214
- Wojtak R., Hjorth J., Hjortlund J. O., 2023, *MNRAS*, **525**, 5187

## APPENDIX A: POSTERIOR DISTRIBUTIONS ON DIFFERENCES BETWEEN MASS BINS

Figures A1 and A2 present joint and marginal posterior distributions on the differences between the parameters inferred for each mass bin for our analysis presented in Section 4.2, included here for completeness. These figures respectively correspond to our models which allow for an intrinsic magnitude offset and a difference in baseline intrinsic SED between SNe Ia in high- and low-mass bins, with a split at  $10^{10} M_{\odot}$ .

## APPENDIX B: ASSESSING COMPLETENESS

To mitigate for the impact of selection effects such as Malmquist bias on our analysis, we have applied upper redshift cuts to the PS1MD and DES3YR samples at  $z < 0.35$  and  $z < 0.4$  respectively. Considering our model, selection effects are most likely to impact inference of the population mean  $A_V$ ,  $\tau_A$  - at higher redshifts, higher extinction objects with large  $A_V$  values are less likely to be observed as they will be fainter in the observer-frame. Without mitigating for selection effects, lower values of  $\tau_A$  will be inferred.

To assess our redshift cuts, we re-run our hierarchical model on the DES3YR and PS1MD samples with lower redshift cuts to examine the impact on the results. The results of this analysis are shown in Table B1. For the DES3YR sample, lowering the upper redshift limit from 0.4 to 0.35 or 0.3 does not impact the inferred value of  $\tau_A$ . This provides reassurance that with our chosen redshift limit of 0.4, the sample is not significantly impacted by selection effects. Our findings are similar for the PS1MD sample; a redshift cut at 0.3 does

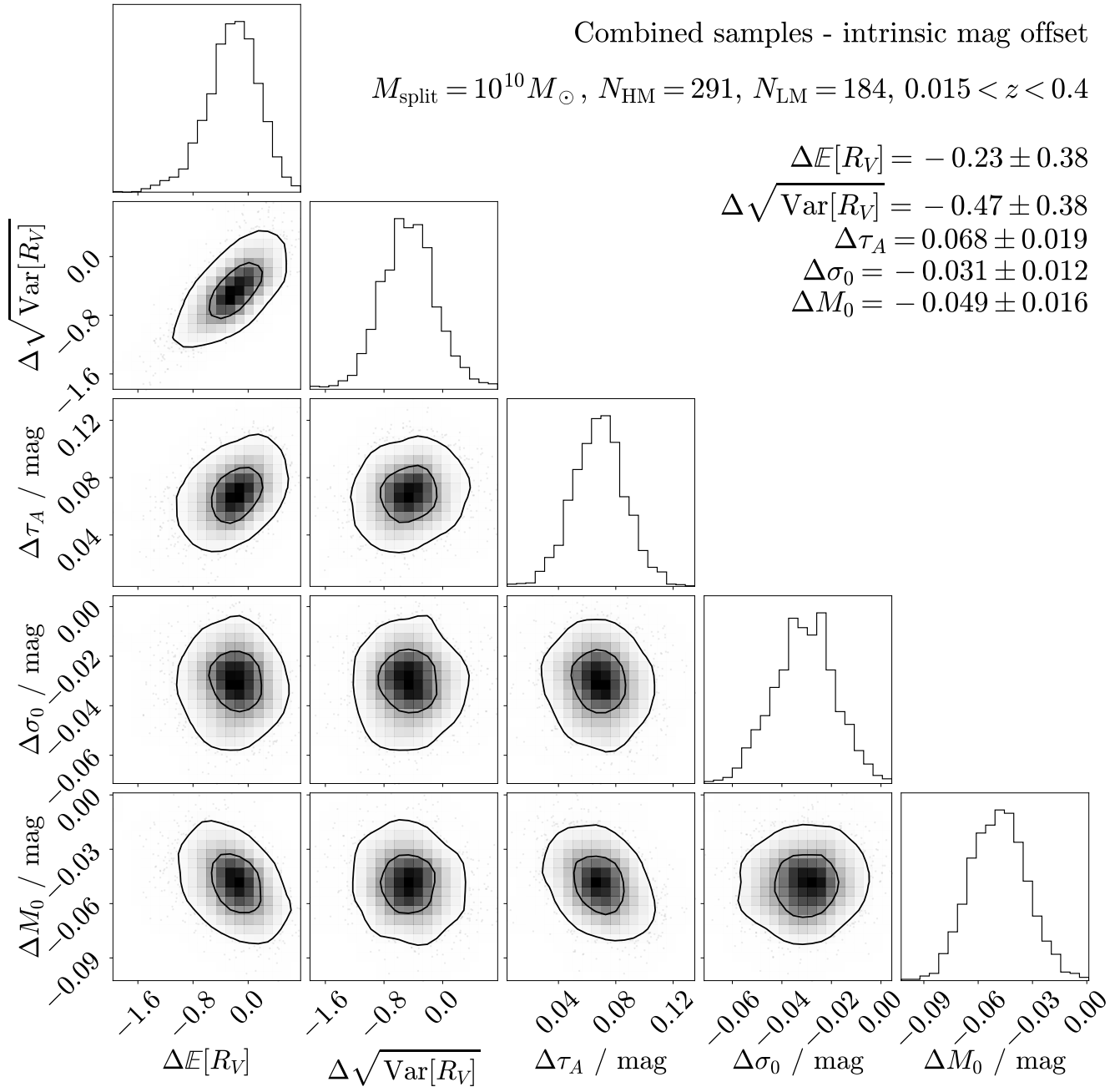


**Figure A1.** Joint and marginal posterior distributions for the difference between inferred parameter values of  $\mu_R$ ,  $\sigma_R$ ,  $\tau_A$ ,  $\Delta M_0$  and  $\sigma_0$  in high- and low-mass bins. These are for the model which allows for an intrinsic magnitude offset between each mass bin in addition to different host galaxy dust distributions.

not impact the inferred  $\tau_A$  value, and while an even lower cut at 0.25 does increase the inferred value by  $\sim 0.01$  mag this difference is not statistically significant.

To further verify that our redshift cuts are reasonable, we also consider the inferred  $A_V$  values when fitting these samples with the BayeSN model trained in [Thorp et al. \(2021\)](#) as a function of redshift. These results are shown in [Figure B1](#). For each redshift bin, we combine all posterior samples on  $A_V$  across all SNe in the bin, calculate the mean and standard error on the mean for each posterior sample, and then calculate the mean across all posterior samples for

these two statistics; these are the plotted values and uncertainties (with the exception of the lowest redshift bin for DES3YR, denoted by a star, in which there is only one SN and hence the plotted error bar corresponds to the posterior standard deviation on that single value.). It should be noted that many of these posteriors will only be upper limits meaning that a point estimate may not be the most appropriate summary statistic, but the mean in each bin remains useful as a first order tool to examine how  $A_V$  varies with redshift. Considering the DES3YR sample, shown in the middle panel of [Figure B1](#), we do not see evidence for a clear decrease in  $A_V$  with redshift below  $z = 0.4$ ;

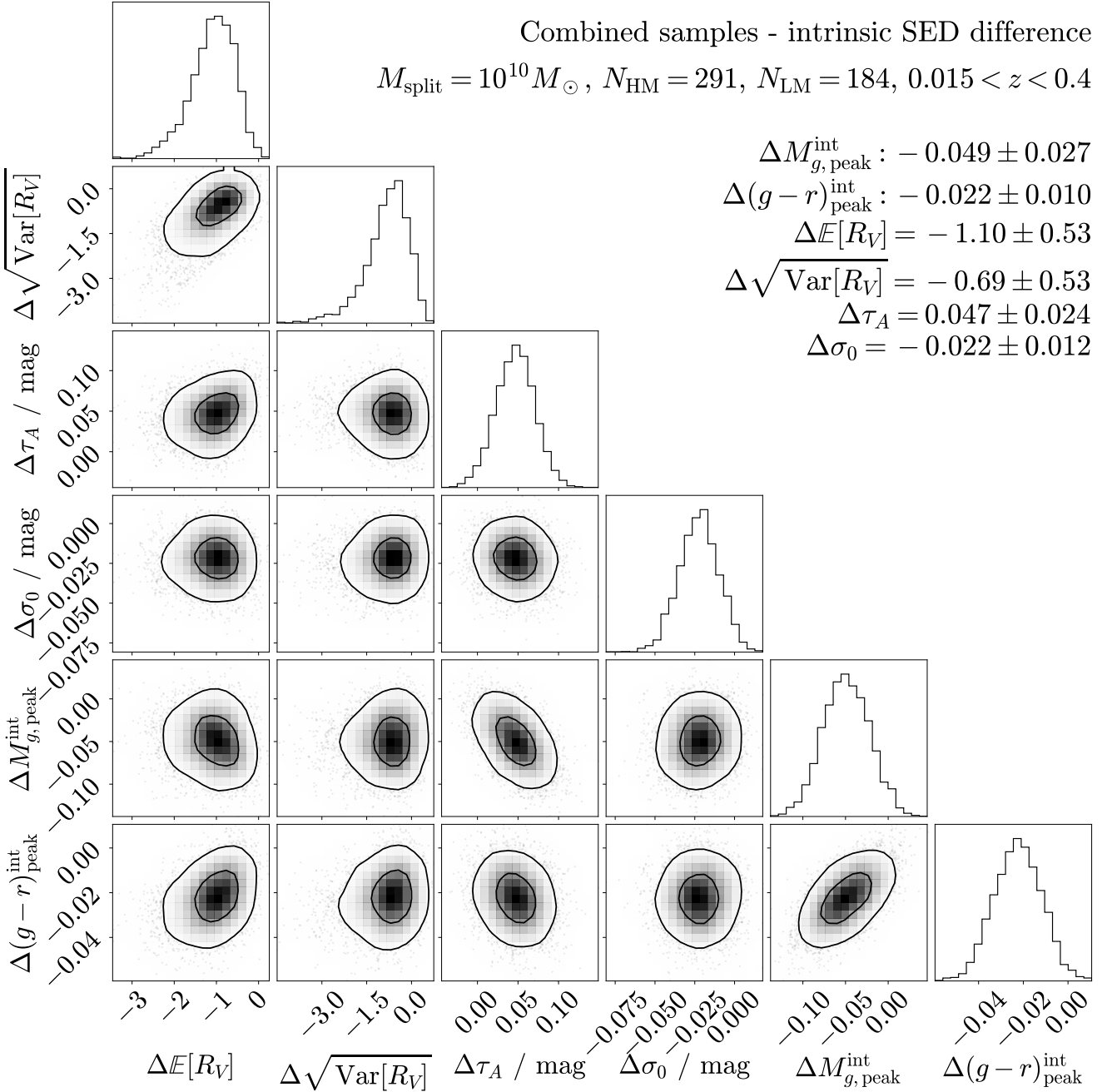


**Figure A2.** Joint and marginal posterior distributions for the difference between inferred parameter values of  $\mathbb{E}[R_V]$ ,  $\sqrt{\text{Var}[R_V]}$ ,  $\tau_A$  and  $\sigma_0$ , as well as derived baseline intrinsic peak  $g$ -band absolute magnitude and  $g-r$  colour, in high- and low-mass bins. These are for the model which allows for a difference in baseline intrinsic SED between each mass bin in addition to different host galaxy dust distributions.

as mentioned previously, the single, higher  $A_V$  bin denoted by a star at the lowest redshift corresponds to a single object. For the PS1MD sample, shown in lower panel of Figure B1,  $A_V$  remains consistent with redshift between  $0.15 < z < 0.35$ . While some of the lowest redshift bins do have higher  $A_V$  values they also contain fewer SNe.

Overall, we are confident that our samples are not significantly impacted by selection effects, although we cannot rule out the possibility that some small effect may remain.

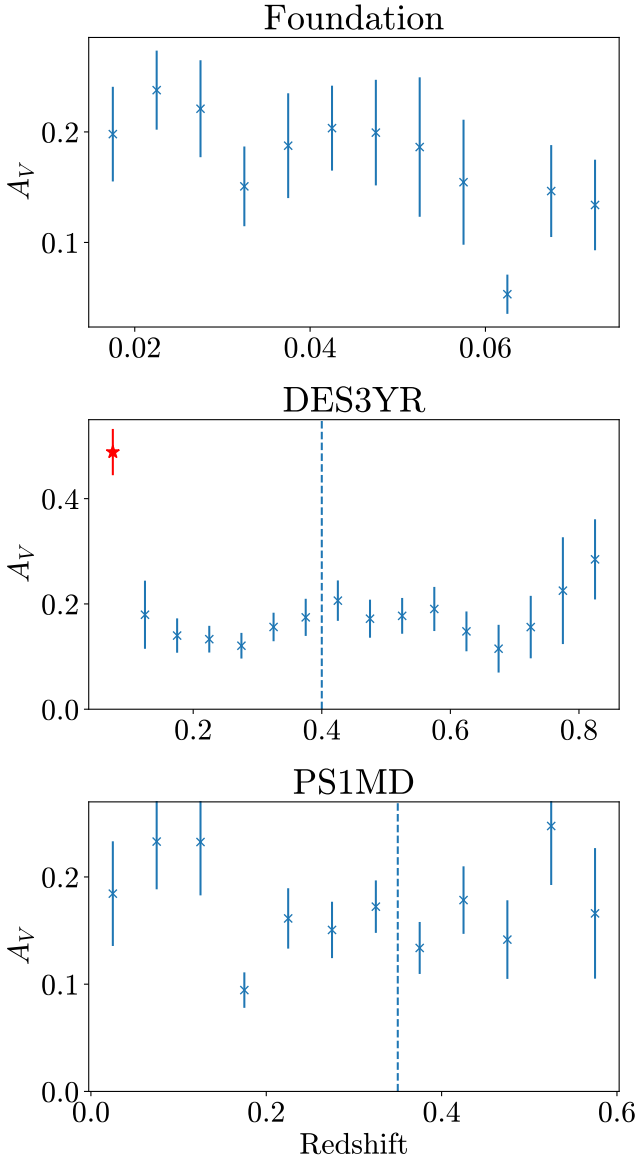
### APPENDIX C: MEAN AND VARIANCE OF TRUNCATED NORMAL DISTRIBUTIONS

As discussed in Section 3.2.3, a truncated normal distribution  $x \sim TN(\mu, \sigma^2, a, b)$  will not in fact have a population mean and variance  $\mu$  and  $\sigma^2$  - these represent the mean and variance of a normal distribution prior to truncation between  $a$  and  $b$ . Instead, the population mean of a truncated normal distribution is given by,

$$\mathbb{E}[x] = \mu + \frac{\phi(\alpha) - \phi(\beta)}{\Phi(\beta) - \Phi(\alpha)} \sigma \quad (\text{C1})$$

**Table B1.** Inferred  $\tau_A$  values using our hierarchical dust model for the DES3YR and PS1MD samples with different upper redshift cuts.

Survey	Upper redshift limit	$N_{SN}$	$\tau_A$ / mag
DES3YR	0.3	65	$0.138 \pm 0.022$
–	0.35	98	$0.140 \pm 0.018$
–	0.40	119	$0.142 \pm 0.017$
PS1MD	0.25	108	$0.148 \pm 0.017$
–	0.3	147	$0.133 \pm 0.015$
–	0.35	198	$0.137 \pm 0.013$

**Figure B1.** Redshift-binned  $A_V$  posterior sample mean and standard error on the mean based on BayeSN fits using the model trained in [Thorpe et al. \(2021\)](#) for each of the Foundation, DES3YR and Foundation samples. Dashed lines for DES3YR and PS1MD indicate the upper redshift limit of the volume limited sub-samples included in our analysis. The lowest redshift bin for DES3YR, denoted by a star, includes only a single object and therefore we plot the posterior standard deviation for that object rather than a standard error on the mean.

while the variance is given by,

$$\text{Var}[x] = \sigma^2 \left[ 1 - \frac{\beta\phi(\beta) - \alpha\phi(\alpha)}{\Phi(\beta) - \Phi(\alpha)} - \left( \frac{\phi(\alpha) - \phi(\beta)}{\Phi(\beta) - \Phi(\alpha)} \right)^2 \right]. \quad (\text{C2})$$

In these definitions,  $\alpha \equiv \frac{a-\mu}{\sigma}$  and  $\beta \equiv \frac{b-\mu}{\sigma}$ . The function  $\phi(y)$  is the probability density function of the standard normal distribution,

$$\phi(y) = \frac{1}{\sqrt{2\pi}} \exp\left(-\frac{y^2}{2}\right) \quad (\text{C3})$$

and the function  $\Phi(y)$  is the cumulative density function of the standard normal distribution,

$$\Phi(y) = \frac{1}{2} (1 + \text{erf}(y/\sqrt{2})) \quad (\text{C4})$$

where  $\text{erf}(z)$  is the error function.

In this work, we set  $b = \infty$ , meaning that  $\phi(\beta) = 0$  and  $\Phi(\beta) = 1$ . Properties of the truncated normal distribution can be found at: [https://people.sc.fsu.edu/~jburkardt/presentations/truncated\\_normal.pdf](https://people.sc.fsu.edu/~jburkardt/presentations/truncated_normal.pdf) (Burkardt 2014).

#### APPENDIX D: POST-PROCESSING MASS SPLIT MODEL WITH INTRINSIC SED DIFFERENCES

Equation 1 gives an expression for the BayeSN model. It should be noted that if we apply the following transforms to the BayeSN model,

$$\theta_1^s \rightarrow \theta_1^s - A \quad W_0(t, \lambda_r) \rightarrow W_0(t, \lambda_r) + AW_1(t, \lambda_r) \quad (\text{D1})$$

where  $A$  is an arbitrary constant, the resulting model is identical because the extra terms of  $AW_1(t, \lambda_r)$  will cancel. As a result, a shift in  $W_0(t, \lambda_r)$  which is proportional to  $W_1(t, \lambda_r)$  will correspond to a shift in the mean of the  $\theta_1$  distribution, which can be set arbitrarily. When the model is trained, we place a prior  $\theta_1^s \sim N(0, 1)$  and the model will create its own consistent definition of  $\theta_1$  relative to  $W_0(t, \lambda_r)$  across the SN population.

However, a complication arises when allowing for intrinsic SED differences between SNe Ia in different mass bins as in Section 3.3.2. In the BayeSN model,  $\theta_1$  acts as a stretch parameter representing the evolutionary timescale of the SN around peak. It is well established that SNe in higher mass galaxies have higher stretch values; we expect the mean of the  $\theta_1$  distribution for the high-mass bin,  $\bar{\theta}_{1,\text{HM}}$ , to be greater than the mean for the low-mass bin,  $\bar{\theta}_{1,\text{LM}}$ . However, when we allow  $W_0(t, \lambda_r)$  to vary between mass bins we are also implicitly allowing for the mean  $\theta_1$  value to vary between mass bins, because of the transformation properties described above. Since we place a prior  $\theta_1^s \sim N(0, 1)$ ,  $\Delta W^m$  will shift to separately set the mean of the  $\theta_1$  distribution for each bin to be close to zero. However, we know that there is a physical difference in the mean  $\theta_1$  between the two bins so  $\theta_1 = 0$  in the high-mass bin will not correspond to the same light curve shape as  $\theta_1 = 0$  in the low-mass bin.

The easiest way to consider this difference is to relate it to an observable property e.g.  $\Delta m_{15}$ . We want a given value of  $\theta_1$  to correspond to a given value of  $\Delta m_{15}$ , regardless of whether the SN is in the high-mass bin or the low-mass bin. In the  $W_0$  split model, this is no longer necessarily the case. To give an example of why this comparison won't work, consider the following example:

- In a model without a  $W_0$  split, consider one SN in each mass bin. The SN in the low-mass bin has a latent  $\theta_1^s = -0.3$ , corresponding to  $\Delta m_{15} = 0.7$  mag. The SN in the high-mass bin, meanwhile, has a latent  $\theta_1^s = 0.0$ , corresponding to  $\Delta m_{15} = 0.8$  mag. Of course, in

reality, we have posterior distributions rather than fixed values, but for the sake of simplicity in this example we consider fixed values.

- Now we switch to a model which does have a  $W_0$  split. As we have allowed  $W_0$  to vary, there have been corresponding linear shifts in the  $\theta_1$  distribution in each mass bin.

- For this new model, for the SN in the high-mass bin there has been no shift and we still infer  $\theta_1^s = 0.0$ . However, for the low-mass bin there has been a shift and for the SN in this bin we now infer  $\theta_1^s = 0.0$ , since the mean of the  $\theta_1$  distribution has been increased by 0.3. Of course, this SN still has the same physical properties, with  $\Delta m_{15} = 0.7$  mag.

- If we are to naively evaluate the baseline intrinsic SED in each mass bin by setting  $\theta_1^s = A_V^s = \epsilon^s(t, \lambda_r) = 0$ , we are in fact comparing the SED for two different stretch values – we are comparing a SN with  $\Delta m_{15} = 0.7$  mag in the low-mass bin with a SN from the high-mass bin that has  $\Delta m_{15} = 0.8$  mag, not making a like-for-like comparison.

To ensure a fair comparison between high- and low-mass bins, we must apply some post-processing to the MCMC chains for  $\Delta W^m$  to ensure that a single value of  $\theta_1^s$  maps to the same value of  $\Delta m_{15}$  for both mass bins. As previously shown, the model is invariant under a linear shift in  $\theta_1$  and corresponding shift in  $W_0$ , therefore we can adjust  $W_0$  to ensure this condition is met. For this work, we adjust  $\Delta W^m$  such that for both mass bins  $\Delta m_{15}$  in  $g$ -band  $\Delta m_{g,15} = 0.8$  mag. This choice is arbitrary although does not impact our results.

- For each mass bin, we compute an updated  $W_0^m(t, \lambda_r) = W_0(t, \lambda_r) + \Delta W^m(t, \lambda_r)$  where  $W_0(t, \lambda_r)$  is the original  $W_0$  matrix for the T21 BayeSN model.

- We use  $W_0^m(t, \lambda_r)$  to compute  $\Delta m_{g,15}^m$  in  $g$ -band, then calculate the difference between this and our reference value of 0.8 mag.

- We calculate the gradient  $\frac{\partial \Delta m_{g,15}^m}{\partial \theta_1}$ , which depends only on  $W_1$  and is therefore the same between both mass bins since this parameter is kept fixed.

- We use the difference and gradient from above to calculate the correction in  $\theta_1$  which will ensure  $\Delta m_{g,15}(\theta_1 = 0) = 0.8$  mag. Overall, for each mass bin we shift the  $\theta_1$  distribution such that  $\theta_1^{s,m} \rightarrow \theta_1^{s,m} - \theta_{1,\text{corr}}^m$  and in turn  $W_0^m(t, \lambda_r) \rightarrow W_0^m(t, \lambda_r) + \theta_{1,\text{corr}}^m W_1(t, \lambda_r)$

The gradient  $\frac{\partial \Delta m_{g,15}^m}{\partial \theta_1}$  can be calculated simply using the autodiff functionality of JAX. Alternatively, an analytic expression can be derived as shown in Appendix E. Strictly speaking, this gradient is weakly dependent on  $\theta$ , however in practice the variation is negligible over a reasonable range of  $\theta$  values and we used the value for the model from Thorp et al. (2021) of  $\frac{\partial \Delta m_{g,15}^m}{\partial \theta_1} |_{\theta_1=0} = 0.1408^6$ . The expression for the correction factor on  $\theta_1$  outlined above is therefore

$$\theta_{1,\text{corr}}^m = \frac{\Delta m_{g,15}^m(\theta = 0) - 0.8}{0.1408} \quad (\text{D2})$$

This process is followed for every step along the chain to give a posterior distribution on  $W_0^m(t, \lambda_r)$  with a consistent definition of  $\theta_1$  across both bins. We can then set  $\theta_1^s = A_V^s = \epsilon^s(t, \lambda_r) = 0$  to do a like-for-like comparison between the baseline intrinsic SED for each mass bin.

## APPENDIX E: RELATING THE 15 DAY DECLINE IN MAG TO BAYESN'S SHAPE PARAMETER

In this appendix we will derive an expression for the derivative of  $\Delta m_{g,15} = m_g(t = 15 \text{ d}) - m_g(t = 0 \text{ d})$ , with respect to BAYESN's light curve shape parameter  $\theta_1$ . Although we will write down this expression for the  $g$ -band, it can be applied to any passband.

The  $g$ -band apparent magnitude of a supernova at a rest frame phase  $t$  is given by

$$m_g(t) = -2.5 \log_{10}[f_g(t)] + Z \quad (\text{E1})$$

where  $Z$  is the zero-point, and  $f_g(t)$  is the BAYESN model flux (see Mandel et al. 2022 eq. 4 and 6). The decline in rest-frame  $g$ -band magnitude in the 15 days after peak is given by

$$\Delta m_{g,15} = m_g(t = 15 \text{ d}) - m_g(t = 0 \text{ d}) \quad (\text{E2})$$

$$= -2.5 \log_{10} \left[ \frac{f_g(t = 15 \text{ d})}{f_g(t = 0 \text{ d})} \right] \quad (\text{E3})$$

$$= -\frac{2.5}{\ln 10} \ln \left[ \int_{\lambda \in g} S(t = 15 \text{ d}, \lambda) \mathbb{B}_g(\lambda) \lambda \, d\lambda \right] + \frac{2.5}{\ln 10} \ln \left[ \int_{\lambda \in g} S(t = 0 \text{ d}, \lambda) \mathbb{B}_g(\lambda) \lambda \, d\lambda \right], \quad (\text{E4})$$

where  $\lambda$  is rest-frame wavelength,  $\mathbb{B}_g(\lambda)$  is the transmission function for the  $g$ -band (normalised as in eq. 3 of Mandel et al. 2022), and  $S(t, \lambda)$  is the BAYESN model SED. With no dust extinction ( $A_V = 0$ ) and no residual variation ( $\epsilon(t, \lambda) = 0$ ), the model SED is given by

$$S(t, \lambda) = S_0(t, \lambda) 10^{-0.4[M_0 + W_0(t, \lambda) + \theta_1 W_1(t, \lambda)]}. \quad (\text{E5})$$

A factor of  $10^{-0.4M_0}$  can easily be cancelled from both integrals in the expression for  $\Delta m_{g,15}$ . We are interested in the gradient of the  $\Delta m_{g,15}$  vs.  $\theta_1$  relation, i.e.  $d(\Delta m_{g,15})/d\theta_1$ . Differentiating one of the terms in the expression for  $\Delta m_{g,15}$  w.r.t.  $\theta_1$ , we find

$$\frac{d}{d\theta_1} \ln \left[ \int_{\lambda \in g} S(t, \lambda) \mathbb{B}_g(\lambda) \lambda \, d\lambda \right] = \frac{\int_{\lambda \in g} \frac{\partial S(t, \lambda)}{\partial \theta_1} \mathbb{B}_g(\lambda) \lambda \, d\lambda}{\int_{\lambda \in g} S(t, \lambda) \mathbb{B}_g(\lambda) \lambda \, d\lambda}, \quad (\text{E6})$$

where

$$\frac{\partial S(t, \lambda)}{\partial \theta_1} = -\frac{\ln 10}{2.5} W_1(t, \lambda) S(t, \lambda). \quad (\text{E7})$$

Therefore, the derivative of interest is given by

$$\frac{d(\Delta m_{g,15})}{d\theta_1} = \frac{\int_{\lambda \in g} W_1(t = 15 \text{ d}, \lambda) S(t = 15 \text{ d}, \lambda) \mathbb{B}_g(\lambda) \lambda \, d\lambda}{\int_{\lambda \in g} S(t = 15 \text{ d}, \lambda) \mathbb{B}_g(\lambda) \lambda \, d\lambda} - \frac{\int_{\lambda \in g} W_1(t = 0 \text{ d}, \lambda) S(t = 0 \text{ d}, \lambda) \mathbb{B}_g(\lambda) \lambda \, d\lambda}{\int_{\lambda \in g} S(t = 0 \text{ d}, \lambda) \mathbb{B}_g(\lambda) \lambda \, d\lambda} \quad (\text{E8})$$

This paper has been typeset from a  $\text{\TeX}/\text{\LaTeX}$  file prepared by the author.

<sup>6</sup> After post-processing, at  $\theta_1 = 0$  the values of  $\Delta m_{g,15}^m$  are consistent for each mass bin to approximately 0.01 per cent.